

Oden Institute REPORT 20-03

February 2020

Analysis of non-conforming DPG methods on polyhedral meshes using fractional Sobolev norms

by

C. Bacuta, L. Demkowicz, J. Mora Paz, and Ch. Xenophontos



Oden Institute for Computational Engineering and Sciences
The University of Texas at Austin
Austin, Texas 78712

Reference: C. Bacuta, L. Demkowicz, J. Mora Paz, and Ch. Xenophontos, "Analysis of non-conforming DPG methods on polyhedral meshes using fractional Sobolev norms," Oden Institute REPORT 20-03, Oden Institute for Computational Engineering and Sciences, The University of Texas at Austin, February 2020.

Analysis of non-conforming DPG methods on polyhedral meshes using fractional Sobolev norms

C. Bacuta^a, L. Demkowicz^b, J. Mora Paz^{b1} and Ch. Xenophontos^c

^aDepartment of Mathematics, University of Delaware

^bOden Institute, The University of Texas at Austin

^cDepartment of Mathematics and Statistics, University of Cyprus

Abstract

The work is concerned with two problems: a) analysis of a DPG method set up in fractional energy spaces, b) use of the results to investigate a non-conforming version of the DPG method for general, polyhedral meshes. We use the ultraweak variational formulation for the model Laplace equation. The theoretical estimates are supported with 3D numerical experiments.

1 Introduction

Model problem. The presented work is concerned with the analysis of a non-conforming version of the *Discontinuous Petrov-Galerkin (DPG) Method with Optimal Test Functions* based on the *Ultraweak (UW) variational formulation*. We shall focus on the model Poisson problem,

$$\begin{cases} -\Delta u = f & \text{in } \Omega \\ u = 0 & \text{on } \Gamma \end{cases}$$

where $\Omega \subset \mathbb{R}^N$ is a Lipschitz domain with boundary Γ , and $N = 2, 3$. The UW formulation derives from the equivalent system of first order equations,

$$\begin{cases} \sigma - \nabla u = 0 & \text{in } \Omega \\ -\operatorname{div} \sigma = f & \text{in } \Omega \\ u = 0 & \text{on } \Gamma \end{cases}$$

which can be represented concisely in the operator form,

$$Au = f.$$

Here $u := (\sigma, u)$ is a group variable, $f = (0, f)$, and

$$Au = A(\sigma, u) = (\sigma - \nabla u, -\operatorname{div} \sigma).$$

More precisely,

$$A : \mathbb{L}^2(\Omega) \supset D(A) \rightarrow \mathbb{L}^2(\Omega)$$

¹Corresponding author: jdmorap@utexas.edu

is a closed operator with

$$D(A) := \{(\sigma, u) \in \mathbf{L}^2(\Omega); A(\sigma, u) \in \mathbf{L}^2(\Omega), u = 0 \text{ on } \Gamma\} = H(\operatorname{div}, \Omega) \times H_0^1(\Omega),$$

where $\mathbf{L}^2(\Omega) := L^2(\Omega)^N \times L^2(\Omega)$. The UW variational formulation is obtained by multiplying both equations with test functions τ, v and integrating by parts *both* equations. We obtain,

$$\begin{cases} \mathbf{u} \in \mathbf{L}^2(\Omega) \\ (\mathbf{u}, A^* \mathbf{v}) = (\mathbf{f}, \mathbf{v}) \quad \mathbf{v} \in D(A^*). \end{cases} \quad (1.1)$$

Here A^* is the \mathbf{L}^2 -adjoint of operator A ,

$$\begin{aligned} A^* &: \mathbf{L}^2(\Omega) \supset D(A^*) \rightarrow \mathbf{L}^2(\Omega) \\ A^* \mathbf{v} &= A(\tau, v) = (\tau + \nabla v, \operatorname{div} \tau) \in \mathbf{L}^2(\Omega) \\ D(A^*) &= D(A). \end{aligned}$$

The *broken UW formulation* is obtained by testing with test functions from a larger space of *broken* test functions $V(\mathcal{T}_h) := H(\operatorname{div}, \mathcal{T}_h) \times H^1(\mathcal{T}_h)$. This necessitates introducing additional unknowns - the Lagrange multipliers, called *traces*,

$$\begin{cases} \mathbf{u} \in \mathbf{L}^2(\Omega), \hat{\mathbf{u}} := (\hat{\sigma}_n, \hat{u}) \in H^{-1/2}(\Gamma_h) \times \tilde{H}^{1/2}(\Gamma_h) \\ (\mathbf{u}, A_h^* \mathbf{v}) - \langle \hat{\mathbf{u}}, \mathbf{v} \rangle_{\Gamma_h} = (\mathbf{f}, \mathbf{v}) \quad \mathbf{v} \in V(\mathcal{T}_h). \end{cases} \quad (1.2)$$

Here \mathcal{T}_h denotes a partition of the domain into finite elements, whose set of interfaces (or skeleton) is Γ_h and

$$\langle \hat{\mathbf{u}}, \mathbf{v} \rangle_{\Gamma_h} = \sum_{K \in \mathcal{T}_h} [\langle \hat{\sigma}_n, v \rangle_{\partial K} + \langle \hat{u}, \tau \cdot n \rangle_{\partial K}].$$

Trace $\hat{\sigma}_n$ is defined by taking a function from $H(\operatorname{div}, \Omega)$, restricting it to each element $K \in \mathcal{T}_h$, and taking its normal trace on element boundary ∂K . Similarly, trace \hat{u} is obtained by taking a function from $H_0^1(\Omega)$, restricting it to each element K , and taking its trace on ∂K . The ‘‘tilde’’ symbol hides the boundary condition on trace \hat{u} ,

$$\tilde{H}^{1/2}(\Gamma_h) := \{\hat{u} \in H^{1/2}(\Gamma_h) : \hat{u} = 0 \text{ on } \Gamma\}.$$

It has been shown in [13] that problem (1.2) is well-posed.

The broken UW formulation is perhaps the least demanding formulation in terms of global conformity. The L^2 space is discretized with discontinuous functions, and so are the broken test spaces. The trace space $H^{-1/2}(\Gamma_h)$ is discretized with traces of Raviart-Thomas elements, i.e. with discontinuous functions over faces e in the mesh skeleton Γ_h . Only the discretization of \hat{u} , done with traces of H^1 -conforming elements, requires a global continuity over the element faces.

The numerical approximation to the solution of (1.2) implies a non-symmetric functional setting and answering the question if the discrete version of the problem is well-posed. To this end, the DPG finite element methodology, explained next, offers a framework that may solve this model problem, and any other variational problem that fits into the abstract setting that we now present.

DPG: Discontinuous Petrov-Galerkin with optimal test functions. Suppose that we have the following abstract variational problem: find $\mathbf{u} \in \mathcal{U}$ such that

$$b(\mathbf{u}, \mathbf{v}) = \ell(\mathbf{v}) \quad \forall \mathbf{v} \in \mathcal{V}, \quad (1.3)$$

where both trial space \mathcal{U} and test space \mathcal{V} are real Hilbert spaces, $\ell \in \mathcal{V}'$, and $b(\cdot, \cdot) : \mathcal{U} \times \mathcal{V} \rightarrow \mathbb{R}$ is a bilinear continuous functional, with continuity constant M , that satisfies the inf-sup condition

$$\inf_{\mathbf{u} \in \mathcal{U}} \sup_{\mathbf{v} \in \mathcal{V}} \frac{|b(\mathbf{u}, \mathbf{v})|}{\|\mathbf{u}\|_{\mathcal{U}} \|\mathbf{v}\|_{\mathcal{V}}} = \gamma > 0. \quad (1.4)$$

The energy norm $\|\cdot\|_E$ on \mathcal{U} is defined as follows:

$$\|\mathbf{u}\|_E = \sup_{\mathbf{v} \in \mathcal{V}} \frac{|b(\mathbf{u}, \mathbf{v})|}{\|\mathbf{v}\|_{\mathcal{V}}}. \quad (1.5)$$

Let $\mathcal{B} : \mathcal{U} \rightarrow \mathcal{V}'$ be a linear operator defined by $\mathcal{B}\mathbf{u} := b(\mathbf{u}, \cdot)$; then (1.5) is equivalent to

$$\|\mathbf{u}\|_E = \sup_{\mathbf{v} \in \mathcal{V}} \frac{|\langle \mathcal{B}\mathbf{u}, \mathbf{v} \rangle|}{\|\mathbf{v}\|_{\mathcal{V}}} = \|\mathcal{B}\mathbf{u}\|_{\mathcal{V}'}. \quad (1.6)$$

The ideal DPG method: The ideal DPG method is a minimum residual FE method that delivers the best approximation error in the energy norm (1.5). This is equivalent to minimizing the residual in the dual test space norm (by virtue of (1.6)). More precisely, given a discrete trial subspace $\mathcal{U}^h \subset \mathcal{U}$ with dimension N_h , the ideal DPG solution $\mathbf{u}_h \in \mathcal{U}^h$ satisfies

$$\|\mathbf{u} - \mathbf{u}_h\|_E = \inf_{\mathbf{w}_h \in \mathcal{U}^h} \|\mathbf{u} - \mathbf{w}_h\|_E = \inf_{\mathbf{w}_h \in \mathcal{U}^h} \|\mathcal{B}(\mathbf{u} - \mathbf{w}_h)\|_{\mathcal{V}'} = \inf_{\mathbf{w}_h \in \mathcal{U}^h} \|\ell - \mathcal{B}\mathbf{w}_h\|_{\mathcal{V}'}. \quad (1.7)$$

where $\mathbf{u} \in \mathcal{U}$ is the exact solution to (1.3). Now, let $\mathcal{R}_{\mathcal{V}} : \mathcal{V} \rightarrow \mathcal{V}'$ be the Riesz map of \mathcal{V} associated with norm $\|\cdot\|_{\mathcal{V}}$. Then,

$$\|\mathbf{u} - \mathbf{u}_h\|_E = \inf_{\mathbf{w}_h \in \mathcal{U}^h} \|\mathcal{R}_{\mathcal{V}}^{-1}(\ell - \mathcal{B}\mathbf{w}_h)\|_{\mathcal{V}}. \quad (1.8)$$

By working out the minimization problem in (1.8), the ideal DPG corresponds to the following Petrov-Galerkin formulation [27]: find $\mathbf{u}_h \in \mathcal{U}^h$ such that

$$b(\mathbf{u}_h, \mathbf{v}_h) = \ell(\mathbf{v}_h) \quad \forall \mathbf{v}_h \in \mathcal{V}^h := \mathbf{T}\mathcal{U}^h \subset \mathcal{V}, \quad (1.9)$$

where $\mathbf{T} : \mathcal{U} \rightarrow \mathcal{V}$ is the *trial-to-test* map, defined by $\mathbf{T} := \mathcal{R}_{\mathcal{V}}^{-1}\mathcal{B}$. The functions in \mathcal{V}^h are known as *optimal test functions* because they automatically grant discrete stability to this Petrov-Galerkin discretization. The following stability estimate holds for the solution of (1.9) [27]:

$$\|\mathbf{u} - \mathbf{u}_h\|_{\mathcal{U}} \leq \frac{M}{\gamma_h} \inf_{\mathbf{w}_h \in \mathcal{U}^h} \|\mathbf{u} - \mathbf{w}_h\|_{\mathcal{U}} \leq \frac{M}{\gamma} \inf_{\mathbf{w}_h \in \mathcal{U}^h} \|\mathbf{u} - \mathbf{w}_h\|_{\mathcal{U}}, \quad (1.10)$$

where $\gamma_h \geq \gamma$ is the discrete inf-sup constant of the bilinear functional b .

Remark 1 For our model problem, we can identify the ingredients of the ideal abstract DPG method as follows: \mathbf{u} is the trial group variable $(\mathbf{u}, \hat{\mathbf{u}}) = (\sigma, u, \hat{\sigma}_n, \hat{u})$; \mathbf{v} is the test group variable $\mathbf{v} = (\tau, v)$; the trial space is $\mathcal{U} = \mathbb{L}^2(\Omega) \times H^{-1/2}(\Gamma_h) \times \tilde{H}^{1/2}(\Gamma_h)$, while the (broken) test space is $\mathcal{V} = H(\text{div}, \mathcal{T}_h) \times H^1(\mathcal{T}_h)$; the bilinear functional $b(\mathbf{u}, \mathbf{v})$ and the linear operator $\ell(\mathbf{v})$ are the left-hand side and right-hand side of the equation in (1.2), respectively. Constants M and γ are found in [26, 35]. ■

DPG in practice: Unless we are dealing with a very special test space, for which inverting its Riesz map $\mathcal{R}_{\mathcal{V}}$ is feasible, in general this problem is infinite-dimensional, so it is impossible to solve without some approximation. Hence we need to work with a finite-dimensional *enriched test space* $\mathcal{V}^r \subsetneq \mathcal{V}$ rather than with the whole space. The dimension of this space is $N_r \geq N_h$. To obtain the so-called practical DPG method, the only required modification to (1.9) is to replace \mathbf{T} by its discrete counterpart $\mathbf{T}^r := (\mathcal{R}_{\mathcal{V}^r})^{-1} \iota^{\top} \mathcal{B}$, that maps trial functions into the enriched test space; here, $\mathcal{R}_{\mathcal{V}^r}$ is the Riesz map of \mathcal{V}^r and ι^{\top} is the transpose of the inclusion $\iota : \mathcal{V}^r \rightarrow \mathcal{V}$.

We may now translate the formulation into an algebraic problem. Let's take a basis of \mathcal{V}^r , $\{\mathbf{v}_k^r\}_{k=1}^{N_r}$; hence the *near-optimal* test functions $\{\mathbf{v}_{i,\text{n-opt}}\}_{i=1}^{N_h}$ can be computed through

$$\mathbf{v}_{i,\text{n-opt}} = \sum_{j,k=1}^{N_r} (\mathbf{B}^{\top})_{ij} (\mathbf{G}^{-1})_{jk} \mathbf{v}_k \quad i = 1, \dots, N_h, \quad (1.11)$$

where \mathbf{B} is called the enriched stiffness matrix, and \mathbf{G} is the Gram matrix of \mathcal{V}^r , defined by

$$\mathbf{B}_{ji} := b(\mathbf{u}_i, \mathbf{v}_j^r), \quad \mathbf{G}_{kj} := (\mathbf{v}_j^r, \mathbf{v}_k^r)_{\mathcal{V}}$$

where $\{\mathbf{u}_i\}_{i=1}^{N_h}$ is a basis for \mathcal{U}^h . Additionally, define the vector \mathbf{l} by $\mathbf{l}_k := \ell(\mathbf{v}_k^r)$. If the numerical solution is written like $\mathbf{u}^h = \sum \mathbf{u}_i d_i$, the coefficient vector \mathbf{d} solves the discrete linear system

$$\mathbf{B}^{\top} \mathbf{G}^{-1} \mathbf{B} \mathbf{d} = \mathbf{B}^{\top} \mathbf{G}^{-1} \mathbf{l}. \quad (1.12)$$

In (1.12), let the left-hand side matrix be denoted $\mathbf{B}^{\text{n-opt}} = \mathbf{B}^{\top} \mathbf{G}^{-1} \mathbf{B}$, which is symmetric and positive definite, and the right-hand side vector by $\mathbf{l}^{\text{n-opt}} = \mathbf{B}^{\top} \mathbf{G}^{-1} \mathbf{l}$, where the n-opt superscript alludes to the near-optimal test functions being utilized. In short, the practical DPG solves the problem $\mathbf{B}^{\text{n-opt}} \mathbf{d} = \mathbf{l}^{\text{n-opt}}$.

The stability of the ideal DPG method is carried over to the practical DPG method if there exists a linear operator $\Pi_F : \mathcal{V} \rightarrow \mathcal{V}^r$, hereinafter referred to as the Fortin operator, satisfying these conditions [35]:

$$\begin{cases} b(\mathbf{u}_h, \mathbf{v} - \Pi_F \mathbf{v}) = 0 & \forall \mathbf{v} \in \mathcal{V}, \mathbf{u}_h \in \mathcal{U}^h \quad (\text{orthogonality}) \\ \|\Pi_F \mathbf{v}\|_{\mathcal{V}} \leq C_F \|\mathbf{v}\|_{\mathcal{V}} & \forall \mathbf{v} \in \mathcal{V} \quad (\text{continuity}) \end{cases} \quad (1.13)$$

Using C_F , the continuity constant of Π_F in (1.13), the estimate (1.10) becomes

$$\|\mathbf{u} - \mathbf{u}_h\|_{\mathcal{U}} \leq \frac{C_F M}{\gamma} \inf_{\mathbf{w}_h} \|\mathbf{u} - \mathbf{w}_h\|_{\mathcal{U}}. \quad (1.14)$$

Remark 2 The abstract presentation above only yields a Petrov-Galerkin method with optimal test functions. The use of broken test functions is what gives DPG its *discontinuous* character. This type of test functions allows to compute $B^{n\text{-opt}}$ locally and then assemble it into a global matrix, instead of assembling G globally and inverting it, which would be a much more expensive process than the actual discrete problem. ■

Polygonal and Polyhedral Finite Element methods. Numerical solutions of boundary value problems (BVPs) with meshes of general polytopes have raised great attention over the last two decades, although the first methods were proposed much earlier by Wachspress [53]. The latter introduced rational barycentric coordinates, which formed a finite element basis over convex polygons, leading to a conforming finite element (FE) method with a new type of element. We can regard this as the first conforming Polygonal FE Method (PFEM), in which a stiffness matrix is computed as in the classical Galerkin formulation, and the theory of approximation is based on the fact that their discrete spaces fulfill some type of global continuity which makes them a subspace of the corresponding infinite-dimensional trial or test space. Precisely here lies a major challenge when working with polytopal elements, as coming up with a conforming finite basis for arbitrary polygonal or polyhedral meshes requires working with non-polynomial functions.

Other generalized barycentric coordinates on polygons, have been used in this FE approach, enabling the use of non-convex elements as well. Within the family of PFEM with generalized barycentric coordinates, we can find methods working with harmonic coordinates [8], entropy coordinates, mean-value coordinates and others [40]. Applications of such methods are known in elasticity, optimization, crack propagation, pervasive fracture, etc. [49, 17, 51, 47, 9]. Research on numerical integration on polytopes, adaptivity with such methods, and higher order spaces has also received attention [50, 42, 18, 46, 34].

Besides PFEM a growing collection of numerical methods that use general polytopes to discretize is now available, and many are built upon principles other than conforming FE methods.

A related class of finite difference (FD) methods, called the Mimetic Finite Difference (MFD) methods, based on mimicking differential operators in a discrete setting, has also been extended successfully to polytopal grids [38, 10, 10]. From the ideas of MFD, a new method with a growing acceptance nowadays has been developed: the Virtual Element Method (VEM). The method avoids explicit construction of shape functions that are conforming to polytopal meshes, but instead tailors spaces that virtually comply with conformity. The virtual shape functions are not accessed directly, but only through their projection onto polynomial spaces. VEM has been applied to a large number of applications and has generated high order approximations of equations of a very diverse nature. Additionally, VEM works with elements with very relaxed regularity assumptions, which makes it really versatile. It does require, however, a stabilization term that is problem-dependent. It cannot deliver its real solution (it is virtual) but only a polynomial projection of it. For representative developments of the subject, see [3, 21, 6, 11, 5, 15, 16, 33, 7, 4].

Other methods include versions of Finite Volume (FV) methods, Discontinuous Galerkin FE methods, or similar approaches that, because of their low-regularity requirements or non-conforming character, can

be extended to elements of arbitrary shape [45, 12, 43, 19, 30]. We fail to mention a number of additional techniques that altogether illustrate that polytopal meshes has become a “hot subject” in numerical analysis.

PolyDPG. DPG has been recently introduced into the family of polygonal methods by Vaziri, Fuentes, Mora and Demkowicz [52], who have labeled their proposed methodology as *PolyDPG*. In 2D, the extension of DPG to polygonal elements has been enabled by the *ultraweak variational formulation* and *broken test spaces*. These two features have allowed for use of discontinuous trial and test functions inside the elements, leaving the connectivity throughout the domain handled only by trace variables defined on the mesh skeleton, which in 2D is simply the union of line segments. The issue of finding a basis of globally continuous basis functions for polygons has thus been avoided. A convergence analysis of the method delivered an optimal error estimate. The theoretical findings have been verified numerically. The highlights of the two-dimensional version of PolyDPG, in contrast to other methods, are that it is a high-order and stable polygonal finite element method, whose ultraweak-conforming discrete spaces are constructed with polynomials only.

Also in 3D, a conforming discretization of trace \hat{u} ought to consist of basis functions that are globally continuous throughout the entire mesh skeleton, which is the union of all the faces. Since traditional elements (tetrahedra, hexahedra, prisms and pyramids) possess triangular and quadrilateral faces only, it is indeed possible to build such discrete spaces (using for instance traces of conforming spaces derived for such element types, such as those in [32]). Even if the element is a more general polyhedron, but with all its faces being triangular or quadrilateral, it is possible to have a piecewise polynomial conforming discrete space for approximating \hat{u} . If this is the case, we could show the convergence of the practical DPG for (1.2) following a procedure similar to the 2D case [52], whenever we have analogous assumptions regarding element shape and Fortin operators.

For general polygonal faces, obtaining such a conforming discrete subspace is not possible with facewise polynomials only (it is a problem as difficult as getting a globally continuous basis for 2D polygonal meshes). A discontinuous polynomial basis is therefore a practical but *non-conforming* way to discretize the subspace for this unknown.

For this reason, we must study the effect on the stability and approximability of the PolyDPG method when choosing a discontinuous basis for the trace \hat{u} . In the literature there are results concerning this situation in DPG when dealing with standard elements, but when the element is an arbitrary polyhedron (which has any number of polygonal faces) the analysis turns more complicated, starting with the fact that there is no unique reference element or unique reference face, so that we need to argue that the error estimates can be independent of the element shape.

Next, we review the main ideas and conclusions from previous work on non-conforming DPG and remark which points are of most interest to us in our analysis.

Existing analysis of non-conforming DPG method. In an early preprint paper on analysis of the DPG method, Demkowicz and Gopalakrishnan presented 2D computations using discontinuous polynomials for

the discretization of all traces, making one of the variables non-conforming. Even though this could be perceived as a “variational crime”, because the analysis was relying on conformity, the numerical results were satisfactory [26]. Noticing this finding, Heuer, Karkulik and Sayas first studied the convergence of a DPG method with discontinuous traces on simplicial meshes [36]. Such analysis delivered the following conclusions:

1. It is possible to furnish the trial space with a weaker norm, and the test space with a stronger norm, such that the continuous problem remains well-posed and the discretization with discontinuous traces gives rise to a conforming DPG method (with respect to the new functional setting).
2. If we wish to keep our original trial norm to measure the error, the analysis shows quasi-optimal convergence for the main unknown only (cf. [36, Theorem 1 and Corollary 2]), while if the trial norm is the *energy norm*, all variables are quasi-optimally controlled by the best approximation error (cf. [36, Remark 9]).
3. The computational implementation is insensitive to the choice of the norms mentioned above, since we can keep computing DPG’s optimal test functions with the Riesz operator corresponding to the original test norm. In other words, the new functional setting is a theoretical artifice necessary for proving convergence, but the practical DPG implementation of (1.12) remains as if we had the original test norm.

In this paper we use their argument to transfer our results in fractional-Sobolev test norms to the integral-Sobolev (original) test norm.

Another relevant development in non-conforming DPG is that by Ernesti and Wieners on space-time DPG for linear wave problems [31]. There, in what the authors call a “simplified DPG method”, the discretization of the traces is made independently over each facet of the tensor-product space-time cells, without enforcing continuity. For the sake of the analysis, it is assumed that there exists a “reconstruction” space, which is a subspace of the local field space such that its traces deliver the same linear system as the non-conforming space. Following this assumption, a new discrete norm is proposed and this allows to transfer the convergence result for a conforming DPG method (cf. [31, Theorem 5.2]) to the non-conforming scenario (cf. [31, Theorem 6.1]). As in the other cited work, here this new subspace is merely virtual, and never used in computations.

Goal, scope and organization of this paper. The present paper is concerned with the stability analysis and a-priori error estimate for a non-conforming version of both the ideal and practical DPG methods for the Poisson problem set up in fractional Sobolev spaces, in which the discretization of trace \hat{u} is done with *discontinuous* polynomials. The rationale behind this endeavor is that, unlike $H^{1/2}$, the fractional spaces that we are considering below contain discontinuous piecewise polynomials, thus this discretization is conforming with respect to the fractional spaces, and the Babuška-Necas theorem provides the stability

for this case. Given the complexity of a computational implementation of fractional norms, all numerical results reported below correspond to the original functional setting, which can be interpreted as the limit case of the fractional setting considered in our theoretical framework.

In Section 2, we start by analyzing the infinite-dimensional scenario of the Poisson model problem formulated in fractional spaces. After introducing the fractional Sobolev spaces and norms, we show that the classical variational formulation is well-posed, which in turn helps proving that the ultraweak variational formulation is well-posed too, as derived in Section 3. Once there, in Section 4 we begin the analysis with broken test spaces and localization of fractional norms, to get to the first major results: the inf-sup condition of the broken ultraweak formulation, and the stability for the ideal DPG with fractional norms (cf. Theorems 2 and 3).

Section 5 deals with the implications of the present analysis on the practical non-conforming DPG. By stating and checking four assumptions (one of them further elaborated on in Appendix A), we get the discrete stability for a DPG method that is computationally implemented with the original integral Sobolev norms, but controlling the error in the weaker fractional norms. This is followed by the analysis on approximability of the discrete trace spaces (Section 6). The ultimate a-priori error estimates herein developed are found in Section 7.

A collection of numerical results of PolyDPG with discontinuous discretization of \hat{u} is presented in section 8, showing a diverse group of polyhedral meshes on which the method works, delivering convergence rates similar to the theoretical ones for some or all the unknowns. The conclusions of the paper are summarized in Section 9.

2 Classical Variational Formulation

Fractional Spaces, Equivalence of Different Fractional Norms. We will move rather freely between different definitions of fractional Sobolev spaces and the corresponding norms. Let $\Omega \subset \mathbb{R}^N$ be a Lipschitz domain. For any $s \in \mathbb{R}$, we define the space $H^s(\Omega)$ as the space of restrictions from $H^s(\mathbb{R}^N)$ with the minimum energy extension norm. Spaces $H^s(\mathbb{R}^N)$ are defined using Bessel potentials, see [41], p.77 or [23], Section 3.1.

For $s = m + \mu$, $m \in \mathbb{N}$, $\mu \in (0, 1)$, we define the space

$$W^s(\Omega) := \{u \in W^m(\Omega) : |D^\alpha u|_{\mu, \Omega} < \infty, \quad |\alpha| = m\}$$

where $|\cdot|_{\mu, \Omega}$ denotes the Slobodeckij seminorm. We equip the space with the scaled norm,

$$\|u\|_{W(\Omega)}^2 := \|u\|_{W^m(\Omega)}^2 + a_\mu^{-1} \sum_{|\alpha|=m} \frac{m!}{\alpha!} |D^\alpha u|_{\mu, \Omega}^2$$

where the scaling coefficient

$$a_\mu = \int_0^\infty t^{-2\mu-1} \int_{|\omega|=1} |e^{i2\pi\omega_1 t} - 1|^2 d\omega dt.$$

Note that the scaling coefficient blows up at $\mu \rightarrow 0, 1$.

We limit now ourselves to $s \in [0, 2]$. One can show that $W^s(\mathbb{R}^N) = H^s(\mathbb{R}^N)$ with equivalent norms and uniformly bounded equivalence constants (a consequence of scaling with a_μ), see [23], Lemma 3.2.1. One can also show the same result for spaces $W^s(\Omega) = H^s(\Omega)$. To prove $W^s(\Omega) \hookrightarrow H^s(\Omega)$ one has to utilize the existence of an extension operator from $W^s(\Omega)$ into $W^s(\mathbb{R}^N)$, see [41], Theorem 3.16 or [23], Theorem 3.2.1. For the operators one can use Calderon operators E_0, E_1, E_2 , see [41], Appendix A, or [23], Theorems 3.4.1 and 3.4.2. Upon ‘‘unpacking the proofs’’ of Theorems 3.4.1, 3.4.2, one learns that extension operator E_0 is uniformly bounded for $s \in [0, 1]$, and so is E_1 for the range $s \in [1, 2]$.

Next comes the (real) interpolation argument. One can show that spaces $H^s(\mathbb{R}^N)$ form an *exact interpolation scale* (the interpolated norm equals the original norm), provided one uses the normalizing factor

$$N_\theta = \left(\frac{2 \sin \pi \theta}{\pi} \right)^{\frac{1}{2}}$$

where $\theta \in (0, 1)$ is the interpolation parameter. We shall implicitly use this factor in all our interpolation arguments. Spaces $H^s(\Omega)$, $s \in [0, 2]$ form also an interpolation scale, although not exact, i.e. , the interpolated and original norms are equivalent but not equal, see [14], Lemma 4.2. Critical in the proof is the existence of *the same* extension operator from $H^s(\Omega)$ into $H^s(\mathbb{R}^N)$, for $s = 0, 2$. This time one can use the Stein operator [48], Section VI.3. If we interpolate between $L^2(\Omega)$ and $H^1(\Omega)$, we might use again Calderon’s E_0 operator.

The interpolation argument allows for the introduction of spectral norms. Let (e_i, λ_i) be the eigenpairs:

$$\begin{cases} e_i \in H^1(\Omega), \lambda_i \in \mathbb{R}_+ \\ (\nabla e_i, \nabla v) + (e_i, v) = \lambda_i (e_i, v) \quad v \in H^1(\Omega). \end{cases}$$

We assume that the eigenvectors have been orthonormalized in the L^2 -norm. The eigenvectors form an orthonormal basis in $L^2(\Omega)$ which allows for the spectral representation,

$$\begin{aligned} u &= \sum_{i=1}^{\infty} u_i e_i, \quad \|u\|^2 = \sum_{i=1}^{\infty} |u_i|^2, \quad u \in L^2(\Omega) \\ \|u\|_{H^1(\Omega)}^2 &= \sum_{i=1}^{\infty} \lambda_i |u_i|^2, \quad u \in H^1(\Omega). \end{aligned}$$

The interpolation argument leads then to the spectral representation for the fractional norms,

$$\|u\|_{H^s(\Omega)}^2 \approx \|u\|_{[L^2(\Omega), H^1(\Omega)]_s}^2 = \sum_{i=1}^{\infty} \lambda_i^s |u_i|^2 =: \|u\|_{\text{sp}H^s(\Omega)}^2.$$

The formula extends to the range $s \in [1, 2]$ if we assume additionally that Ω is convex². Indeed, it is sufficient to see that

$$\|u\|_{H^2(\Omega)}^2 \approx \|u\|_{L^2(\Omega)}^2 + \|\Delta u\|_{L^2(\Omega)}^2 = \sum_i (1 + (\lambda_i - 1)^2) |u_i|^2 \approx \sum_i (1 + \lambda_i^2) |u_i|^2$$

²The assumption can be avoided by employing a more subtle argument based on the subspace interpolation method and restricting the range to $s \in [1, 3/2]$.

and interpolate between $H^1(\Omega)$ and $H^2(\Omega)$.

Finally, we mention that for $s \in [0, s_0]$, $s_0 < \frac{1}{2}$, space $H^{-s}(\Omega)$ can be identified with the dual of space $H^s(\Omega)$ with equivalent norms that are uniformly equivalent, [23], Theorem 3.5.3.

Equivalence³ of $H^{1+s}(\Omega)$ and $H^s(\text{grad}, \Omega)$. It is a straightforward exercise, see [23], Exercise 4.1.1, that the two spaces are identical with equivalent norms, for $\Omega = \mathbb{R}^N$. The equivalence constants are uniformly bounded for a bounded $|s|$. This implies embedding of $H^{1+s}(\Omega)$ into $H^s(\text{grad}, \Omega)$. Indeed, let $U \in H^{1+s}(\mathbb{R}^N)$ be the minimum energy extension of $u \in H^{1+s}(\Omega)$. We have,

$$\|u\|_{H^s(\text{grad}, \Omega)}^2 := \|u\|_{H^s(\Omega)}^2 + \|\nabla u\|_{H^s(\Omega)}^2 \leq \|U\|_{H^s(\mathbb{R}^N)}^2 + \|\nabla U\|_{H^s(\mathbb{R}^N)}^2 \approx \|U\|_{H^{1+s}(\mathbb{R}^N)}^2 = \|u\|_{H^{1+s}(\Omega)}^2.$$

For $s \in (0, 1)$, the reverse inequality is immediate if we switch from minimum energy extension norms $H^s(\Omega)$ to the equivalent $W^s(\Omega)$ -norms. Indeed, it is sufficient to compare the norms,

$$\begin{aligned} \|u\|_{W^{1+s}(\Omega)}^2 &= \|u\|_{W^1(\Omega)}^2 + a_\mu^{-1} \sum_{|\alpha|=1} \|D^\alpha u\|_{\mu, \Omega}^2 \\ \|u\|_{W^s(\text{grad}, \Omega)}^2 &= \|u\|_{W^s(\Omega)}^2 + \|\nabla u\|_{W^s(\Omega)}^2 \\ &= \|u\|_{L^2(\Omega)}^2 + a_\mu^{-1} \|u\|_{\mu, \Omega}^2 + \sum_{|\alpha|=1} \left[\|D^\alpha u\|_{L^2(\Omega)}^2 + a_\mu^{-1} \|D^\alpha u\|_{\mu, \Omega}^2 \right]. \end{aligned}$$

The equivalence of $H^{1-s}(\Omega)$ and $H^{-s}(\text{grad}, \Omega)$ -norms is shown for $s \in (0, s_0)$, $s_0 < \frac{1}{2}$, and it is based on a duality argument.

$$\begin{aligned} \|u\|_{H^{1-s}(\Omega)} &\approx \|u\|_{[L^2(\Omega), H^1(\Omega)]_{1-s}} = \|u\|_{\text{sp}H^{1-s}(\Omega)} \\ &= \|u\|_{(\text{sp}H^{1+s}(\Omega))'} \approx \|u\|_{(H^s(\text{grad}, \Omega))'} \\ &\leq \|u\|_{H^{-s}(\text{grad}, \Omega)}. \end{aligned}$$

The last inequality follows from:

$$\sup_v \frac{|\langle u, v \rangle + \langle \nabla u, \nabla v \rangle|}{(\|v\|_{H^s(\Omega)}^2 + \|\nabla v\|_{H^s(\Omega)}^2)^{1/2}} \leq \|u\|_{H^{-s}(\text{grad}, \Omega)}.$$

Spectral representation of $H_0^{1\pm s}(\Omega)$. Finally, we record a more convenient spectral representation for subspace $H_0^{1\pm s}(\Omega)$, $s \in [0, s_0]$, $s_0 < \frac{1}{2}$. The reasoning is the same as above but we use a different set of eigenpairs,

$$\begin{cases} e_i \in H_0^1(\Omega), \lambda_i \in \mathbb{R}_+ \\ (\nabla e_i, \nabla v) = \lambda_i (e_i, v) \quad v \in H_0^1(\Omega). \end{cases}$$

We get,

$$\|u\|_{H_0^{1\pm s}(\Omega)}^2 \approx \sum_{i=1}^{\infty} \lambda_i^{1\pm s} |u_i|^2. \quad (2.15)$$

³Used in the proof of well-posedness for the UW formulation.

Well-posedness of the classical variational formulation in fractional spaces. Given $\epsilon \in (0, 1/2)$ we consider the following variational formulation of the Poisson problem: Find u such that

$$\begin{cases} u \in H_0^{1-\epsilon}(\Omega) \\ (\nabla u, \nabla v) = (f, v), \quad v \in H_0^{1+\epsilon}(\Omega). \end{cases} \quad (2.16)$$

Then, we can establish the following result.

Lemma 1

Assume that $H_0^{1-\epsilon}(\Omega)$ and $H_0^{1+\epsilon}(\Omega)$ are equipped with the spectral norms given by the right hand side of (2.15), respectively. Then, for any $\epsilon \in (0, 1/2)$, the following estimate holds:

$$\sup_{v \in H_0^{1+\epsilon}(\Omega)} \frac{(\nabla u, \nabla v)}{\|v\|_{H_0^{1+\epsilon}(\Omega)}} = \|u\|_{H_0^{1-\epsilon}(\Omega)}. \quad (2.17)$$

■

Proof: Let $u = \sum_{k=1}^{\infty} u_k e_k \in H_0^{1-\epsilon}$ and $v = \sum_{k=1}^{\infty} v_k e_k \in H_0^{1+\epsilon}$. Then, using the Cauchy-Schwarz inequality,

$$\begin{aligned} (\nabla v, \nabla u) &= (-\Delta v, u) = \sum_{k=1}^{\infty} \lambda_k u_k v_k = \sum_{k=1}^{\infty} \lambda_k^{\frac{1-\epsilon}{2}} u_k \lambda_k^{\frac{1+\epsilon}{2}} v_k \\ &\leq \left(\sum_{k=1}^{\infty} \lambda_k^{1-\epsilon} u_k^2 \right)^{1/2} \left(\sum_{k=1}^{\infty} \lambda_k^{1+\epsilon} v_k^2 \right)^{1/2} \\ &= \|u\|_{H_0^{1-\epsilon}(\Omega)} \|v\|_{H_0^{1+\epsilon}(\Omega)}. \end{aligned} \quad (2.18)$$

To prove the reverse inequality we fix $u = \sum_{k=1}^{\infty} u_k e_k \in H_0^{1-\epsilon}$ and define v_u by

$$v_u = \sum_{k=1}^{\infty} \lambda_k^{-\epsilon} u_k e_k.$$

One can immediately check that $v_u \in H_0^{1+\epsilon}(\Omega)$ and $\|v_u\|_{H_0^{1+\epsilon}(\Omega)} = \|u\|_{H_0^{1-\epsilon}(\Omega)}$. Then

$$\sup_{v \in H_0^{1+\epsilon}(\Omega)} \frac{(\nabla u, \nabla v)}{\|v\|_{H_0^{1+\epsilon}(\Omega)}} \geq \frac{(\nabla u, \nabla v_u)}{\|v_u\|_{H_0^{1+\epsilon}(\Omega)}} = \frac{\sum_{k=1}^{\infty} \lambda_k^{1-\epsilon} u_k^2}{\|u\|_{H_0^{1-\epsilon}(\Omega)}} = \|u\|_{H_0^{1-\epsilon}(\Omega)}.$$

■

3 Ultraweak Variational Formulation

The well-posedness analysis of various variational formulations presented in [22] extends easily to fractional spaces. Let $s \in [0, \frac{1}{2})$. Operator A corresponding to the strong formulation is defined as follows.

$$\begin{aligned} \mathbf{u} &= (\sigma, u) \\ \mathbf{H}^{-s}(\Omega) &= H^{-s}(\Omega)^N \times H^{-s}(\Omega) \\ D(A) &:= H^{-s}(\text{div}, \Omega) \times H_0^{1-s}(\Omega) \subset \mathbf{H}^{-s}(\Omega) \\ A : \mathbf{H}^{-s}(\Omega) \supset D(A) &\rightarrow \mathbf{H}^{-s}(\Omega) \\ Au &:= (\sigma - \nabla u, -\text{div } \sigma) \end{aligned}$$

Its topological transpose is defined on the dual space,

$$\begin{aligned} \mathbf{v} &= (\tau, v) \\ \mathbf{H}^s(\Omega) &= H^s(\Omega)^N \times H^s(\Omega) \\ D(A^*) &:= H^s(\text{div}, \Omega) \times H_0^{1+s}(\Omega) \subset \mathbf{H}^s(\Omega) \\ A^* : \mathbf{H}^s(\Omega) \supset D(A^*) &\rightarrow \mathbf{H}^s(\Omega) \\ A^*\mathbf{v} &:= (\tau + \nabla v, \text{div } \sigma) \end{aligned}$$

Since we intend to pass with $s \rightarrow 0$, we assume a more regular than necessary load $\mathbf{f} = (0, f)$, $f \in L^2(\Omega)$. The UW formulation in the fractional spaces looks now as follows.

$$\begin{cases} \mathbf{u} \in \mathbf{H}^{-s}(\Omega) \\ \langle \mathbf{u}, A^*\mathbf{v} \rangle = \langle \mathbf{f}, \mathbf{v} \rangle \quad \mathbf{v} \in D(A^*) \end{cases} \quad (3.19)$$

where $\langle \cdot, \cdot \rangle$ denotes the duality pairing between $\mathbf{H}^{-s}(\Omega)$ and $\mathbf{H}^s(\Omega)$ and $D(A^*)$ is the subspace of the adjoint graph energy space,

$$\mathbf{H}_{A^*}(\Omega) := \{\mathbf{v} \in \mathbf{H}^s(\Omega) : A^*\mathbf{v} \in \mathbf{H}^s(\Omega)\}.$$

THEOREM 1

The ultraweak variational formulation (3.19) is well-posed. ■

Proof:

Step 1: Operator A is bounded below. Let $\mathbf{l} := (g, f) = Au = A(\sigma, u)$, i.e.,

$$\begin{aligned} \sigma - \nabla u &= g \\ -\text{div } \sigma &= f. \end{aligned} \quad (3.20)$$

Testing the second equation with $v \in H_0^{1+s}(\text{grad}, \Omega) = H_0^{1+s}(\Omega)$, and integrating the left-hand side by parts, we obtain,

$$\langle \sigma, \nabla v \rangle = \langle f, v \rangle \quad v \in H_0^{1+s}(\Omega).$$

Substituting $\sigma = \nabla u + g$, we get,

$$\langle \nabla u, \nabla v \rangle = \langle f, v \rangle - \langle g, \nabla v \rangle \quad v \in H_0^{1+s}(\Omega).$$

In other words, u satisfies the classical variational formulation discussed in the previous section. By the results obtained there, we have

$$\|u\|_{H^{1-s}(\Omega)} \leq C \|f\|_{H^{-s}(\Omega)}.$$

But, simultaneously, from (3.20)₁,

$$\|\sigma\|_{H^{-s}(\Omega)} \leq \|\nabla u\|_{H^{-s}(\Omega)} + \|g\|_{H^{-s}(\Omega)} \leq C \|f\|_{H^{-s}(\Omega)}$$

and, from (3.20)₂,

$$\|\operatorname{div} \sigma\|_{H^{-s}(\Omega)} \leq \|f\|_{H^{-s}(\Omega)}$$

which shows that A is bounded below.

Step 2: Operator A^* is injective. Indeed, following a similar reasoning to the previous step, we first show that $\nabla v = 0$ in $H^s(\Omega)$ which implies that v is a constant. But the homogeneous BC on v implies that v must be zero. Consequently, $\tau = -\nabla v = 0$ as well.

Step 3: We invoke the Closed Range Theorem for Closed Operators that shows that A^* is bounded below with the same constant as operator A . Surjectivity and boundedness below of A^* implies now immediately that the bilinear form in the UW fomulation satisfies the inf-sup condition. Indeed, take any $u \in H^{-s}(\Omega)$. Let $w \in H^s(\Omega)$ be the Riesz representation of functional $\langle u, \cdot \rangle$. Take now the unique $v \in D(A^*)$ such that $A^*v = w$. We have,

$$\langle u, A^*v \rangle = \langle u, w \rangle = \|u\|_{H^{-s}(\Omega)}^2.$$

At the same time,

$$\|v\|_{H_{A^*}(\Omega)} \leq (1 + \alpha^{-1}) \|w\|_{H^s(\Omega)} = (1 + \alpha^{-1}) \|u\|_{H^{-s}(\Omega)}$$

where α is the boundedness below constant for operators A and A^* . Consequently,

$$\frac{\langle u, A^*v \rangle}{\|v\|_{H_{A^*}(\Omega)}} \geq (1 + \alpha^{-1})^{-1} \|u\|_{H^{-s}(\Omega)}.$$

The injectivity of A^* implies that space

$$V_0 := \{v \in D(A^*) : \langle u, A^*v \rangle = 0 \quad \forall u \in H^{-s}(\Omega)\}$$

is trivial and, therefore, the Babuška-Nečas Theorem implies that the UW variational formulation is well-posed. ■

Remark 3 One can follow the reasoning in [22] to show that the well-posedness of the UW formulation implies the well-posedness of the classical formulation. All three discussed formulations: the strong formulation, the classical one, and the UW formulation, are thus simultaneously well-posed. ■

4 Broken UW Variational Formulation

Equivalence of standard and localized fractional norms. Given a quasi-uniform, shape-regular FE mesh \mathcal{T}_h , we introduce the *localized fractional norm*,

$$\|v\|_{H^\epsilon(\mathcal{T}_h)}^2 := \sum_{K \in \mathcal{T}_h} \|v\|_{H^\epsilon(K)}^2. \quad (4.21)$$

The localized norm is obviously bounded by the standard, global norm. The converse is also true, with an expected blow-up as $h \rightarrow 0$.

Lemma 2

There exists a constant C , independent of h such that

$$\|v\|_{H^\epsilon(\Omega)} \leq Ch^{-\epsilon} \|v\|_{H^\epsilon(\mathcal{T}_h)} \quad v \in H^\epsilon(\Omega). \quad (4.22)$$

■

Proof: Let \mathcal{G} denote the family of pairs of neighboring elements (K_1, K_2) ,

$$\mathcal{G} := \{(K_1, K_2) \in \mathcal{T}_h \times \mathcal{T}_h : \bar{K}_1 \cap \bar{K}_2 \neq \emptyset\} \quad G := \bigcup_{(K_1, K_2) \in \mathcal{G}} K_1 \times K_2.$$

Consider the corresponding decomposition⁴,

$$\Omega \times \Omega = G \cup G'.$$

The assumption on shape regularity implies that the number of immediate neighbors for an element is uniformly bounded, i.e. the number of times each element K in the mesh appears as K_1 or K_2 in family \mathcal{G} , is bounded uniformly in K (with constant growing exponentially with dimension N). The assumption on quasi-uniformity implies that there exist constants c_1, c_2 such that

$$c_1 h \leq h_K \leq c_2 h \quad K \in \mathcal{T}_h.$$

This in turn implies that there exists a constant $C > 0$, such that

$$G' \subset \{(x, y) \in \Omega \times \Omega : |x - y| \geq Ch\}.$$

Consider now a pair $(K_1, K_2) \in \mathcal{G}$. We have,

$$\int_{K_1} \int_{K_2} \frac{|u(x) - u(y)|^2}{|x - y|^{N+2\epsilon}} dx dy \leq 2 \int_{K_1} \int_{K_2} \frac{|u(x)|^2}{|x - y|^{N+2\epsilon}} dx dy + 2 \int_{K_1} \int_{K_2} \frac{|u(y)|^2}{|x - y|^{N+2\epsilon}} dx dy.$$

⁴Up to subsets of measure zero.

It is sufficient to focus on estimating one of the integrals only, say,

$$\int_{K_1} |u(x)|^2 \int_{K_2} \frac{1}{|x-y|^{N+2\epsilon}} dy dx.$$

Switching to spherical coordinates, we can estimate the inner integral,

$$\int_{K_2} \frac{1}{|x-y|^{N+2\epsilon}} dy \leq |S_1| \int_{d(x,e)} \frac{1}{r^{N+2\epsilon}} r^{N-1} dr = \frac{|S_1|}{2\epsilon} d(x,e)^{-2\epsilon}$$

where $|S_1|$ is the measure of the unit sphere, and $d(x, e)$ denotes the distance to a hypersurface e separating the two elements, see Fig. 4.1. We extend now u to a function $U \in C_0^\infty(\mathbb{R}^N)$. By Lemma 3.5.5 from [23],

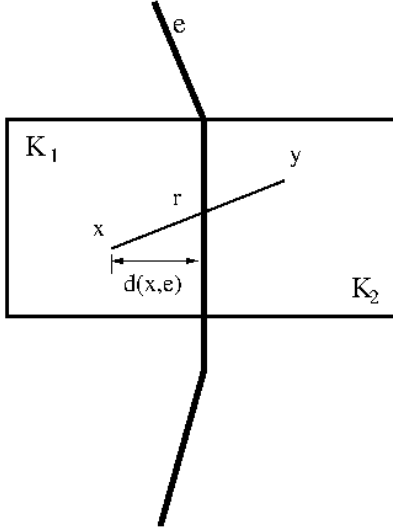


Figure 4.1: Estimation of double integral over two neighboring elements. Notation.

see also Remark 3.5.2 there, there exists a constant $C(\epsilon)$, $C(\epsilon) \rightarrow 1$ as $\epsilon \rightarrow 0$ such that

$$\int_{K_1} |u(x)|^2 d(x, e)^{-2\epsilon} dx \leq C(\epsilon) \|U\|_{H^\epsilon(\mathbb{R}^N)}^2.$$

Passing to the minimum energy extension on the right-hand side, we obtain,

$$\int_{K_1} |u(x)|^2 d(x, e)^{-2\epsilon} dx \leq C(\epsilon) \|u\|_{H^\epsilon(K_1)}^2.$$

The integral over the complementary domain G' is estimated as follows.

$$\begin{aligned} \iint_{G'} \frac{|u(x) - u(y)|^2}{|x-y|^{N+2\epsilon}} dx dy &\leq 2 \iint_{G'} \frac{|u(x)|^2}{|x-y|^{N+2\epsilon}} dx dy + 2 \iint_{G'} \frac{|u(y)|^2}{|x-y|^{N+2\epsilon}} dx dy \\ &= 4 \iint_{G'} \frac{|u(x)|^2}{|x-y|^{N+2\epsilon}} dx dy. \end{aligned}$$

The last integral is now estimated with the L^2 -norm,

$$\begin{aligned} \int_{\Omega} |u(x)|^2 \int_{|x-y|>h} \frac{1}{|x-y|^{N+2\epsilon}} dy dx &\leq \int_{\Omega} |u(x)|^2 \int_h^{\infty} \frac{|S_1|}{r^{N+2\epsilon}} r^{N-1} dr dx \\ &\leq \frac{|S_1|}{2\epsilon} h^{-2\epsilon} \int_{\Omega} |u(x)|^2 dx. \end{aligned}$$

■

Remark 4 For polyhedral elements, the quasi-uniformity assumption on the mesh remains unaltered. However, the shape regularity needs to be understood differently. For the sake of Lemma 2, what matters is to have a uniform bound on the number of immediate neighbors an element can have. An effective way to bound such a quantity is to establish a maximum number of faces per polyhedral element. The higher such maximum is, the larger the equivalence constant may become. ■

Stability analysis for the broken UW variational formulation in fractional spaces. We reformulate now the UW formulation (1.2) in fractional spaces,

$$\begin{cases} \mathbf{u} \in H^{-\epsilon}(\Omega), \hat{\mathbf{u}} := (\hat{\sigma}_n, \hat{\mathbf{u}}) \in H^{-1/2-\epsilon}(\Gamma_h) \times \tilde{H}^{1/2-\epsilon}(\Gamma_h) \\ \langle \mathbf{u}, A_h^* \mathbf{v} \rangle - \langle \hat{\mathbf{u}}, \mathbf{v} \rangle_{\Gamma_h} = (\mathbf{f}, \mathbf{v}) \quad \mathbf{v} \in V^{\epsilon}(\mathcal{T}_h). \end{cases} \quad (4.23)$$

Here $\langle \cdot, \cdot \rangle$ denotes the duality pairing between $H^{-\epsilon}(\Omega)$ and $H^{\epsilon}(\Omega)$, and

$$\begin{aligned} H^{\pm\epsilon}(\Omega) &= H^{\pm\epsilon}(\Omega)^N \times H^{\pm\epsilon}(\Omega) \\ V^{\epsilon}(\mathcal{T}_h) &= H^{\epsilon}(\text{div}, \mathcal{T}_h) \times H^{\epsilon}(\text{grad}, \mathcal{T}_h) \\ H^{-1/2-\epsilon}(\Gamma_h) &= \{ \hat{t} = \{t_K\}_{K \in \mathcal{T}_h} : \exists \sigma \in H^{-\epsilon}(\text{div}, \Omega) : t_K = \gamma_{n, \partial K} \sigma|_K \} \\ H^{1/2-\epsilon}(\Gamma_h) &= \{ \hat{\mathbf{u}} = \{u_K\}_{K \in \mathcal{T}_h} : \exists u \in H^{-\epsilon}(\text{grad}, \Omega) : u_K = \gamma_{\partial K} u|_K \} \end{aligned}$$

with

$$\langle \hat{\mathbf{u}}, \mathbf{v} \rangle_{\Gamma_h} = \sum_{K \in \mathcal{T}_h} \left[\langle \hat{\sigma}_n, v \rangle_{H^{-1/2-\epsilon}(\partial K) \times H^{1/2+\epsilon}(\partial K)} + \langle \hat{\mathbf{u}}, \tau \cdot n \rangle_{H^{1/2+\epsilon}(\partial K) \times H^{-1/2-\epsilon}(\partial K)} \right].$$

The trace spaces defined on the mesh skeleton are equipped with the minimum energy extension norms. The broken test spaces are equipped with the localized test norms derived from (4.21),

$$\begin{aligned} \|\tau\|_{H^{\epsilon}(\text{div}, \mathcal{T}_h)}^2 &:= \sum_{K \in \mathcal{T}_h} \left[\|\tau\|_{H^{\epsilon}(K)}^2 + \|\text{div} \tau\|_{H^{\epsilon}(K)}^2 \right] \\ \|v\|_{H^{\epsilon}(\text{grad}, \mathcal{T}_h)}^2 &:= \sum_{K \in \mathcal{T}_h} \left[\|v\|_{H^{\epsilon}(K)}^2 + \|\text{grad} v\|_{H^{\epsilon}(K)}^2 \right] \end{aligned}$$

Corollary 1 Let $\mathbf{v} \in V^{\epsilon}(\mathcal{T}_h)$ be a broken test function. Lemma 2 implies that the union of $A_h^* \mathbf{v}$ is an element of $H^{\epsilon}(\Omega)$ and,

$$\begin{aligned} |\langle \mathbf{u}, A_h^* \mathbf{v} \rangle| &\leq C \|\mathbf{u}\|_{H^{-\epsilon}(\Omega)} \|A_h^* \mathbf{v}\|_{H^{\epsilon}(\Omega)} \leq Ch^{-\epsilon} \|\mathbf{u}\|_{H^{-\epsilon}(\Omega)} \|A_h^* \mathbf{v}\|_{H^{\epsilon}(\mathcal{T}_h)} \\ &\leq Ch^{-\epsilon} \|\mathbf{u}\|_{H^{-\epsilon}(\Omega)} \|\mathbf{v}\|_{V^{\epsilon}(\mathcal{T}_h)}. \end{aligned} \quad (4.24)$$

The stability analysis follows closely the arguments from [13]. Let

$$l(\mathbf{v}) := \langle \mathbf{u}, A_h^* \mathbf{v} \rangle - \langle \hat{\mathbf{u}}, \mathbf{v} \rangle_{\Gamma_h}.$$

Stability of unbroken UW formulation implies the control of field variable \mathbf{u} ,

$$\begin{aligned} \gamma \|\mathbf{u}\|_{H^{-\epsilon}(\Omega)} &\leq \sup_{\mathbf{v} \in V^\epsilon} \frac{|\langle \mathbf{u}, A_h^* \mathbf{v} \rangle|}{\|\mathbf{v}\|_{V^\epsilon}} \leq \sup_{\mathbf{v} \in V^\epsilon} \frac{|\langle \mathbf{u}, A_h^* \mathbf{v} \rangle|}{\|\mathbf{v}\|_{V^\epsilon(\mathcal{T}_h)}} = \sup_{\mathbf{v} \in V^\epsilon} \frac{|\langle \mathbf{u}, A_h^* \mathbf{v} \rangle - \langle \hat{\mathbf{u}}, \mathbf{v} \rangle_{\Gamma_h}|}{\|\mathbf{v}\|_{V^\epsilon(\mathcal{T}_h)}} \\ &\leq \sup_{\mathbf{v} \in V^\epsilon(\mathcal{T}_h)} \frac{|l(\mathbf{v})|}{\|\mathbf{v}\|_{V^\epsilon(\mathcal{T}_h)}} =: \|l\|_{(V^\epsilon(\mathcal{T}_h))'}. \end{aligned}$$

It follows that,

$$\begin{aligned} \sup_{\mathbf{v} \in V^\epsilon(\mathcal{T}_h)} \frac{|\langle \hat{\mathbf{u}}, \mathbf{v} \rangle_{\Gamma_h}|}{\|\mathbf{v}\|_{V^\epsilon(\mathcal{T}_h)}} &\leq \|l\|_{(V^\epsilon(\mathcal{T}_h))'} + Ch^{-\epsilon} \|\mathbf{u}\|_{H^{-\epsilon}(\Omega)} \\ &\leq (1 + C\gamma^{-1}h^{-\epsilon}) \|l\|_{(V^\epsilon(\mathcal{T}_h))'}. \end{aligned}$$

As in [13], the big question is now whether the quantity on the left represents a norm and how to characterize it. Upon unpacking the duality pairing on the skeleton, we have,

$$\left(\sup_{\mathbf{v} \in V^\epsilon(\mathcal{T}_h)} \frac{|\langle \hat{\mathbf{u}}, \mathbf{v} \rangle_{\Gamma_h}|}{\|\mathbf{v}\|_{V^\epsilon(\mathcal{T}_h)}} \right)^2 = \underbrace{\sum_{K \in \mathcal{T}_h} \left(\|\hat{\sigma}_n\|_{(H^{1/2+\epsilon}(\partial K))'} \right)^2}_{=: \|\hat{\sigma}_n\|_{H^{-1/2-\epsilon}(\Gamma_h)}^2} + \underbrace{\sum_{K \in \mathcal{T}_h} \left(\|\hat{\mathbf{u}}\|_{(H^{-1/2+\epsilon}(\partial K))'} \right)^2}_{=: \|\hat{\mathbf{u}}\|_{H^{1/2-\epsilon}(\Gamma_h)}^2} =: \|\hat{\mathbf{u}}\|^2$$

where the dual norms on the right-hand side are computed with respect to minimum energy extension norms.

$$\begin{aligned} \|\hat{v}\|_{H^{1/2+\epsilon}(\partial K)}^2 &:= \inf_{\text{tr}_{\partial K} v = \hat{v}} \left[\|v\|_{H^\epsilon(K)}^2 + \|\text{grad} v\|_{H^\epsilon(K)}^2 \right] \\ \|\hat{t}\|_{H^{-1/2+\epsilon}(\partial K)}^2 &:= \inf_{\text{tr}_{n, \partial K} \tau = \hat{t}} \left[\|\tau\|_{H^\epsilon(K)}^2 + \|\text{div} \tau\|_{H^\epsilon(K)}^2 \right] \end{aligned} \quad (4.25)$$

It has been shown in [23], Section 4.2, that the dual norms are equivalent to the minimum energy extension norms,

$$\|\hat{\sigma}_n\|_{H^{-1/2-\epsilon}(\partial K)} \quad \text{and} \quad \|\hat{\mathbf{u}}\|_{H^{1/2-\epsilon}(\partial K)}.$$

This implies that the supremum represents indeed a norm. Control of equivalence constants is more delicate. The dual norms are bounded with minimum energy extension norm (with a unit equivalence constant). This will help with the estimation of the best approximation error. However, the estimation of the equivalence constant in the other direction involves a partition of unity argument which makes, a priori, the constant dependent upon the domain (in our case, an element K). Note that, for $\epsilon = 0$, the dual and minimum energy extension norms are equal [13, 23].

We summarize our findings in the following theorem.

THEOREM 2

The following inf-sup condition holds:

$$\min(\gamma, (1 + C\gamma^{-1}h^\epsilon)^{-1}) \left(\|u\|_{H^{-\epsilon}(\Omega)}^2 + \|\hat{u}\|^2 \right)^{\frac{1}{2}} \leq \|I\|_{(V^\epsilon(\mathcal{T}_h))'} = \sup_{v \in V^\epsilon(\mathcal{T}_h)} \frac{|\langle u, A_h v \rangle + \langle \hat{u}, v \rangle_{\Gamma_h}|}{\|v\|_{V^\epsilon(\mathcal{T}_h)}} \quad (4.26)$$

More precisely,

$$\begin{aligned} \gamma \|u\| &\leq \|I\|_{(V^\epsilon(\mathcal{T}_h))'} \\ (C\gamma^{-1}h^{-\epsilon})^{-1} \|\hat{u}\| &\leq \|I\|_{(V^\epsilon(\mathcal{T}_h))'} \end{aligned}$$

■

THEOREM 3

Let (u_h, \hat{u}_h) be the ideal DPG method solution where $\hat{u}_h = (\hat{\sigma}_{n,h}, \hat{u}_h)$.

The following a-priori error estimates hold:

$$\begin{aligned} \gamma \|u - u_h\|_{H^{-\epsilon}(\Omega)} &\leq Ch^{-\epsilon} \inf_{w_h} \|u - w_h\|_{H^{-\epsilon}(\Omega)} \\ &\quad + \left(\sum_{K \in \mathcal{T}_h} \left\{ \inf_{\hat{t}_h} \|\sigma \cdot n - \hat{t}_h\|_{H^{-1/2-\epsilon}(\partial K)}^2 + \inf_{\hat{w}_h} \|u - \hat{w}_h\|_{H^{1/2-\epsilon}(\partial K)}^2 \right\} \right)^{\frac{1}{2}} \end{aligned} \quad (4.27)$$

and

$$\begin{aligned} (1 + C\gamma^{-1}h^{-\epsilon})^{-1} &\left(\sum_{K \in \mathcal{T}_h} \left\{ \|\sigma \cdot n - \hat{\sigma}_{n,h}\|_{(H^{1/2+\epsilon}(\partial K))'}^2 + \|u - \hat{u}_h\|_{(H^{-1/2+\epsilon}(\partial K))'}^2 \right\} \right)^{\frac{1}{2}} \\ &\leq Ch^{-\epsilon} \inf_{w_h} \|u - w_h\|_{H^{-\epsilon}(\Omega)} \\ &\quad + \left(\sum_{K \in \mathcal{T}_h} \left\{ \inf_{\hat{t}_h} \|\sigma \cdot n - \hat{t}_h\|_{H^{-1/2-\epsilon}(\partial K)}^2 + \inf_{\hat{w}_h} \|u - \hat{w}_h\|_{H^{1/2-\epsilon}(\partial K)}^2 \right\} \right)^{\frac{1}{2}}. \end{aligned} \quad (4.28)$$

■

Proof: We only need to recall continuity estimate (4.24) and use the bound:

$$\left| \sum_{K \in \mathcal{T}_h} (\langle \hat{\sigma}_n, v \rangle_{\partial K} + \langle \hat{u}, \tau \cdot n \rangle_{\partial K}) \right| \leq \left(\sum_{K \in \mathcal{T}_h} (\|\hat{\sigma}_n\|_{H^{-1/2-\epsilon}(\partial K)}^2 + \|\hat{u}\|_{H^{1/2-\epsilon}(\partial K)}^2) \right)^{\frac{1}{2}} \|v\|_{V^\epsilon(\mathcal{T}_h)}.$$

■

5 Implications for the Non-conforming DPG Method

In the preceding sections we have developed a theory for a DPG method formulated in fractional spaces. By weakening the trial norm and strengthening the test norm, we have been able to employ the discontinuous discretization of traces which, in the relaxed energy setting, has become conforming. The discussed results

require computations with the stronger, fractional test norm which is not attractive at all from the practical point of view.

In this section, we show how one can combine arguments developed in [36] to conclude semioptimal convergence results in the weaker, fractional $H^{-\epsilon}$ norms, *computing with the standard test norm*. In other words, we change the analysis but not the computations.

We begin by recalling the results from [36] formulated in an abstract form. We assume that we can introduce an alternate functional setting with a stronger test norm $\|v\|_{\mathcal{V}}$, and a weaker trial norm $\|u\|_{\mathcal{U}}$,

$$\|v\|_V \leq \|v\|_{\mathcal{V}} \quad v \in \mathcal{V} \subset V \quad \text{and} \quad \|u\|_{\mathcal{U}} \leq \|u\|_U \quad u \in U \subset \mathcal{U}.$$

We postulate now that the following conditions are satisfied.

Assumption 1: Inf-sup condition in the modified setting,

$$\tilde{\gamma} \|u\|_{\mathcal{U}} \leq \sup_{v \in \mathcal{V}} \frac{|b(u, v)|}{\|v\|_{\mathcal{V}}}.$$

Assumption 2: Existence of Fortin operators for the *stronger* test norm, leading to the discrete stability in the weaker norm,

$$\frac{\tilde{\gamma}}{C_F} \|u_h\|_{\mathcal{U}} \leq \sup_{v_h \in V_r} \frac{|b(u_h, v_h)|}{\|v_h\|_{\mathcal{V}}} \leq \sup_{v_h \in V_r} \frac{|b(u_h, v_h)|}{\|v_h\|_V} \quad u_h \in U_h \subset \mathcal{U}.$$

Assumption 3: Continuity of the bilinear form on the finite-dimensional enriched test space,

$$|b(u, v_h)| \leq M_r \|u\|_{\mathcal{U}} \|v_h\|_V \quad v_h \in V_r \subset \mathcal{V}.$$

Assumption 4: Galerkin orthogonality,

$$b(u_h - u, v) = 0 \quad u \in \mathcal{U}, u_h \in U_h \subset \mathcal{U}, v \in \mathbf{T}^r(U_h)$$

where $\mathbf{T}^r : U \rightarrow V_r$ is the approximate trial-to-test operator corresponding to the original test norm.

With the four assumptions satisfied, we can use now the standard Strang's argument to establish the following a-priori estimate in the weaker norm.

$$\begin{aligned} \|u - u_h\|_{\mathcal{U}} &\leq \|u - w_h\|_{\mathcal{U}} + \|w_h - u_h\|_{\mathcal{U}} && \text{(triangle inequality)} \\ &\leq \|u - w_h\|_{\mathcal{U}} + \frac{C_F}{\tilde{\gamma}} \sup_{v_h \in V_r} \frac{|b(w_h - u_h, v_h)|}{\|v_h\|_V} && \text{(discrete stability)} \\ &= \|u - w_h\|_{\mathcal{U}} + \frac{C_F}{\tilde{\gamma}} \sup_{v_h \in \mathbf{T}^r(U_h)} \frac{|b(w_h - u_h, v_h)|}{\|v_h\|_V} && \text{(definition of optimal test functions)} \\ &= \|u - w_h\|_{\mathcal{U}} + \frac{C_F}{\tilde{\gamma}} \sup_{v_h \in \mathbf{T}^r(U_h)} \frac{|b(w_h - u, v_h)|}{\|v_h\|_V} && \text{(Galerkin orthogonality)} \\ &\leq \left(1 + \frac{C_F}{\tilde{\gamma}} M_r\right) \|u - w_h\|_{\mathcal{U}}. \end{aligned}$$

We now verify the assumptions.

- The inf-sup condition for the fractional setting has been proved in Theorem 2. Inf-sup constant $\tilde{\gamma}$ is of order h^ϵ . For the fields alone, the inf-sup constant is of order one.
- Construction of the Fortin operators has been delegated to Appendix A. For tetrahedral meshes, we are able to employ any of the existing H^1 Fortin operators and, following [36], the standard Raviart-Thomas interpolation operator for the $H(\text{div})$ Fortin operator. Moreover, the construction extends to arbitrary polyhedral meshes, provided we use tetrahedral subelement meshes to define the enriched spaces. Due the scaling properties of the fractional norm, the Fortin constant is of order $h^{-\epsilon}$.
- The continuity of the bilinear form for enriched space test functions is based on the finite-dimensionality argument. For instance,

$$\begin{aligned}
\|\tau\|_{H^\epsilon(T)}^2 &\lesssim h^{-1-2\epsilon} \|\tilde{\tau}\|_{H^\epsilon(\tilde{T})}^2 && \text{(scaling for Piola transform)} \\
&\lesssim C(r) h^{-1-2\epsilon} \|\tilde{\tau}\|_{L^2(\tilde{T})}^2 && \text{(finite dimensionality argument)} \\
&\lesssim C(r) h^{-2\epsilon} \|\tau\|_{L^2(T)}^2 && \text{(scaling for Piola transform)}.
\end{aligned}$$

The norm equivalence constant clearly depends upon the order r of the enriched space, but for limited range of ϵ , it can be claimed to be independent of ϵ . In the end, the continuity constant is $M_r \approx C(r) h^{-2\epsilon}$. One factor h^ϵ is lost due to the scaling properties discussed above, the other comes from the global continuity estimate (4.24).

- The Galerkin orthogonality condition is clearly satisfied.

THEOREM 4

Let $(\mathbf{u}_h, \hat{\mathbf{u}}_h)$ be the practical DPG method solution where $\hat{\mathbf{u}}_h = (\hat{\sigma}_{n,h}, \hat{u}_h)$.

The following a-priori error estimates hold.

$$\begin{aligned}
&\|\mathbf{u} - \mathbf{u}_h\|_{\mathbf{H}^{-\epsilon}(\Omega)} \leq \\
&C(\epsilon) h^{-3\epsilon} \left\{ \inf_{\mathbf{w}_h} \|\mathbf{u} - \mathbf{w}_h\|_{\mathbf{H}^{-\epsilon}(\Omega)} + \left(\sum_{K \in \mathcal{T}_h} [\inf_{\hat{t}_h} \|\sigma \cdot n - \hat{t}_h\|_{H^{-1/2-\epsilon}(\partial K)}^2 + \inf_{\hat{w}_h} \|u - \hat{w}_h\|_{H^{1/2-\epsilon}(\partial K)}^2] \right)^{\frac{1}{2}} \right\} \\
&\hspace{15em} (5.29)
\end{aligned}$$

and

$$\begin{aligned}
&\left(\sum_{K \in \mathcal{T}_h} \{ \|\sigma \cdot n - \hat{\sigma}_{n,h}\|_{(H^{1/2+\epsilon}(\partial K))'}^2 + \|u - \hat{u}_h\|_{(H^{-1/2+\epsilon}(\partial K))'}^2 \} \right)^{\frac{1}{2}} \\
&\leq C(\epsilon) h^{-4\epsilon} \left\{ \inf_{\mathbf{w}_h} \|\mathbf{u} - \mathbf{w}_h\|_{\mathbf{H}^{-\epsilon}(\Omega)} + \left(\sum_{K \in \mathcal{T}_h} [\inf_{\hat{t}_h} \|\sigma \cdot n - \hat{t}_h\|_{H^{-1/2-\epsilon}(\partial K)}^2 + \inf_{\hat{w}_h} \|u - \hat{w}_h\|_{H^{1/2-\epsilon}(\partial K)}^2] \right)^{\frac{1}{2}} \right\}. \\
&\hspace{15em} (5.30)
\end{aligned}$$

Above, $\epsilon \in (0, \frac{1}{2})$ and stability constant $C(\epsilon) \rightarrow \infty$ as $\epsilon \rightarrow 0$. \blacksquare

6 Best Approximation Error Estimates for Polyhedral Elements

6.1 Best Approximation Error Estimate for the Minimum Energy Extension $H^{1/2-\epsilon}$ Norm

The philosophy of developing the best approximation error estimates mirrors the classical approach for finite elements. We move to a master element, apply the Bramble-Hilbert argument, and pullback to the physical element with the proper power of element size resulting from scaling the Sobolev seminorms. There are several delicate steps in the derivations presented next. First of all, all norms equivalence arguments are to be executed only on the master element. In this way, we employ a number of constants that depend upon the master element but not a particular physical element. Secondly, contrary to standard meshes with affine elements, we are dealing not with a single master element but rather a family of “unit” finite elements of different shape and number of faces. Hence we have to make perhaps a “hand-waving” assumption that the constants are uniformly bounded for all our “master elements”.

Given an element K , we begin with the estimation of the norm dual to the minimum energy extension norm $\|\tau \cdot n\|_{H^{-1/2+\epsilon}(\partial K)}$,

$$\|u\|_{(H^{-1/2+\epsilon}(\partial K))'} = \sup_{\tau \in H^\epsilon(\operatorname{div}, K)} \frac{|\langle u, \tau \cdot n \rangle_{\partial K}|}{\|\tau\|_{H^\epsilon(\operatorname{div}, K)}}.$$

Let $u \in H^{1/2-\epsilon}(\partial K)$ and let $U \in H^\epsilon(\operatorname{grad}, K)$ be an arbitrary lift of u . We have,

$$\begin{aligned} (*) &:= \left(\sup_{\tau \in H^\epsilon(\operatorname{div}, K)} \frac{|\langle u, \tau \cdot n \rangle_{\partial K}|}{\|\tau\|_{H^\epsilon(\operatorname{div}, K)}} \right)^2 = \left(\sup_{\tau \in H^\epsilon(\operatorname{div}, K)} \frac{|\langle U, \operatorname{div} \tau \rangle + \langle \nabla U, \tau \rangle|}{(\|\tau\|_{H^\epsilon(K)}^2 + \|\operatorname{div} \tau\|_{H^\epsilon(K)}^2)^{1/2}} \right)^2 \\ &= \left(\sup_{\check{\tau} \in H^\epsilon(\operatorname{div}, \check{K})} \frac{|\langle \check{U}, \check{\operatorname{div}} \check{\tau} \rangle + \langle \check{\nabla} \check{U}, \check{\tau} \rangle|}{(h^{-1} \|\check{\tau}\|_{L^2(\check{K})}^2 + h^{-1+2\epsilon} \|\check{\tau}\|_{H^\epsilon(\check{K})}^2 + h^{-3} \|\check{\operatorname{div}} \check{\tau}\|_{L^2(\check{K})}^2 + h^{-3+2\epsilon} \|\check{\operatorname{div}} \check{\tau}\|_{H^\epsilon(\check{K})}^2)^{1/2}} \right)^2 \\ &\leq \left(\sup_{\check{\tau} \in H^\epsilon(\operatorname{div}, \check{K})} \frac{|\langle \check{U}, \check{\operatorname{div}} \check{\tau} \rangle + \langle \check{\nabla} \check{U}, \check{\tau} \rangle|}{(h^{-1+2\epsilon} \|\check{\tau}\|_{H^\epsilon(\check{K})}^2 + h^{-3+2\epsilon} \|\check{\operatorname{div}} \check{\tau}\|_{H^\epsilon(\check{K})}^2)^{1/2}} \right)^2 \end{aligned}$$

Above, element \check{K} is a unit element (with $h_{\check{K}} = 1$) obtained by translation and simple scaling of element K of size h . We employ the standard Piola transforms for the exact sequence elements,

$$U = \check{U}, \quad E = h^{-1} \check{E}, \quad \tau = h^{-2} \check{\tau}, \quad f = h^{-3} \check{f}.$$

Note that $(U, f)_K = (\check{U}, \check{f})_{\check{K}}$ and $(E, \tau)_K = (\check{E}, \check{\tau})_{\check{K}}$ for (regular) functions. The scaling extends to duality pairing by a density argument or, equivalently, by using it as a definition of transform for elements $U \in H^{-\epsilon}(\operatorname{grad}, K)$ and $E \in H^{-\epsilon}(\operatorname{curl}, K)$.

We follow with the estimation,

$$(*) \leq h^{3-2\epsilon} \|\check{U}\|_{H^{-\epsilon}(\check{K})}^2 + h^{1-2\epsilon} \|\check{\nabla} \check{U}\|_{H^{-\epsilon}(\check{K})}^2 \leq h^{1-2\epsilon} \|\check{U}\|_{H^{-\epsilon}(\operatorname{grad}, \check{K})}^2$$

Consequently, the original dual norm is estimated with the minimum energy extension norm of \check{u} ,

$$(*) \leq h^{1-2\epsilon} \|\check{u}\|_{H^{1/2-\epsilon}(\partial\check{K})}^2.$$

We employ now the localization argument,

$$h^{1-2\epsilon} \|\check{u}\|_{H^{1/2-\epsilon}(\partial\check{K})}^2 \leq C(\epsilon) \sum_{\check{F} \subset \partial\check{K}} \|\check{u}\|_{H^{1/2-\epsilon}(\check{F})}^2$$

where the summation extends over all faces \check{F} of the unit element. Constant $C(\epsilon)$ blows up at rate ϵ^{-1} (see [25]), and it does depend upon the topology and shape of the unit element.

We need to define now an approximation $u_p \in \mathcal{P}^p(F)$ of u . Face F is shared by two elements that may be scaled (slightly) differently, yielding two different master faces \check{F} . However, the assumption on quasi-uniformity of the mesh implies the equivalence of $H^{1/2-\epsilon}(\check{F})$ norms with mesh independent equivalence constants. Hence, we may set \check{u}_p to be the projection of \check{u} in the $H^{1/2-\epsilon}(\check{F})$ norm using one of the two master faces \check{F} ,

$$\check{u}_p := \arg \min_{\check{w}_p \in \mathcal{P}^p(\check{F})} \|\check{u} - \check{w}_p\|_{H^{1/2-\epsilon}(\check{F})}.$$

Employing the Bramble-Hilbert argument, we get,

$$\begin{aligned} \left(\sup_{\tau \in H^\epsilon(\text{div}, K)} \frac{|\langle u - u_p, \tau \cdot n \rangle_{\partial K}|}{\|\tau\|_{H^\epsilon(\text{div}, K)}} \right)^2 &\leq C(\epsilon) h^{1-2\epsilon} \sum_{\check{F}} \inf_{\check{w}_p} \|\check{u} - \check{w}_p\|_{H^{1/2-\epsilon}(\check{F})}^2 \\ &\leq C(\epsilon) h^{1-2\epsilon} \sum_{\check{F}} \inf_{\check{w}_p} \|\check{u} - \check{w}_p\|_{H^r(\check{F})}^2 \\ &\leq C(r) C(\epsilon) h^{1-2\epsilon} \sum_{\check{F}} |\check{u}|_{H^r(\check{F})}^2 \\ &\leq C(r) C(\epsilon) h^{2r-1-2\epsilon} \sum_F |u|_{H^r(F)}^2 \end{aligned}$$

for any $r \leq p+1$. $C(r)$ is the Bramble-Hilbert constant or, more precisely, the maximum constant for all the involved faces. For the maximum $r = p+1$ this leads to the expected rate of convergence,

$$\sup_{\tau \in H^\epsilon(\text{div}, K)} \frac{|\langle u - u_p, \tau \cdot n \rangle_{\partial K}|}{\|\tau\|_{H^\epsilon(\text{div}, K)}} \leq C(r) C(\epsilon) h^{p+\frac{1}{2}-\epsilon} \left(\sum_F |u|_{H^{p+1}(F)}^2 \right)^{1/2}. \quad (6.31)$$

If we limit ourselves to less regular functions $u \in H^{p+\frac{1}{2}}(F)$, by using a (non-trivial) interpolation argument we obtain the expected $h^{p-\epsilon}$ rate of convergence.

For different elements K , we obtain the corresponding, different unit ‘‘master’’ elements \check{K} . In order to make the derived estimate useful, we have to assume that the class of the unit elements we obtain, is either finite or that the corresponding localization constant $C(\epsilon)$ and Bramble-Hilbert constant $C(r)$ are *uniformly bounded* in \check{K} .

6.2 Best Approximation Error Estimate for the Minimum Energy Extension $H^{-1/2}$ Norm

This time we use a different idea. We introduce a polyhedral $H(\text{div})$ -conforming finite element with an “infinite number of bubbles” and develop an interpolation error estimate for such an element. Let $L^2_{\text{avg}}(K)$ denote the subspace of $L^2(K)$ functions with zero average,

$$L^2_{\text{avg}}(K) := \left\{ q \in L^2(K) : \int_K q = 0 \right\}.$$

Lemma 3

Let K be an arbitrary polyhedron with flat faces F .

1. For every $q \in L^2_{\text{avg}}(K)$, there exists a bubble $\sigma \in H_0(\text{div}, K)$ such that $\text{div } \sigma = q$.
2. For every face F , and an arbitrary $t \in \mathcal{P}^{p-1}(F)$, there exists a function $\sigma \in H(\text{div}, K)$ such that normal trace $\sigma \cdot n = t$ on the face F , and it vanishes on the remaining faces.

■

Proof:

1. Consider the Neumann problem,

$$\begin{cases} U \in H^1(K) \\ \int_K \nabla U \cdot \nabla V = \int_K q V \quad V \in H^1(K) \end{cases}$$

and take $\sigma = -\nabla U$.

2. Consider the Neumann problem,

$$\begin{cases} U \in H^1(K) \\ \int_K \nabla U \cdot \nabla V + UV = \int_F t V \quad V \in H^1(K) \end{cases}$$

and take $\sigma = -\nabla U$. Note that $\text{div } \sigma = -\Delta U = -U \in L^2(K)$.

■

We introduce now a “finite element” with the FE space defined as

$$V^p(K) := \{ \sigma \in H(\text{div}, K) : \sigma \cdot n \in \mathcal{P}^{p-1}(F), \text{ for every face } F \subset \partial K \}. \quad (6.32)$$

and the corresponding *Projection-Based (PB) Interpolant* [29] $\sigma_p \in V^p(K)$, $\sigma_p = \Pi\sigma$ defined as follows.

$$\begin{cases} \|\sigma_p \cdot n - \sigma \cdot n\|_{L^2(F)} \rightarrow \min & \text{for every face } F \subset \partial K \\ \|\operatorname{div}(\sigma_p - \sigma)\|_{L^2(K)} \rightarrow \min \\ (\sigma - \sigma_p, \nabla \times E)_K = 0 & E \in H_0(\operatorname{curl}, K) \end{cases} \quad (6.33)$$

for sufficiently regular functions σ . By Lemma 3, the FE space is well defined, and $\operatorname{div} \sigma_p = \operatorname{div} \sigma$. Indeed, condition (6.33)₂ implies that

$$(\operatorname{div}(\sigma_p - \sigma), q) = 0 \quad \text{for every } q \in L^2_{\operatorname{avg}}(K).$$

At the same time, condition (6.33)₁ implies that

$$\int_K \operatorname{div}(\sigma_p - \sigma) = \int_{\partial K} (\sigma_p - \sigma) \cdot n = 0.$$

The $H(\operatorname{div})$ -norm of the interpolation error reduces thus just to the L^2 -norm. Let $\sigma \in H(\operatorname{div}, K)$ be now a sufficiently regular function defined on a polyhedral element K . As usual, we pullback σ to the master element \check{K} , determine the PB interpolant $\check{\sigma}$ there and push it forward to element K . We proceed with the standard derivation of the interpolation error.

$$\begin{aligned} \|\sigma - \sigma_p\|_{L^2(K)} &= h^{-1/2} \|\check{\sigma} - \check{\sigma}_p\|_{L^2(\check{K})} \\ &= h^{-1/2} \|(\check{I} - \check{\Pi})\check{\sigma}\|_{L^2(\check{K})} \\ &= h^{-1/2} \|(\check{I} - \check{\Pi})(\check{\sigma} - \check{\tau}_p)\|_{L^2(\check{K})} && \text{(polynomial preservation property)} \\ &\leq h^{-1/2} \|\check{I} - \check{\Pi}\|_{\mathcal{L}(H^r(\check{K}), L^2(\check{K}))} \|\check{\sigma} - \check{\tau}_p\|_{H^r(\check{K})} \end{aligned}$$

for any polynomial $\check{\tau}_p \in \mathcal{P}^{p-1}(\check{K})^3$, and $r \leq p$. We finish by applying the Bramble-Hilbert and scaling arguments,

$$\|\sigma - \sigma_p\|_{L^2(K)} \leq Ch^{-1/2} \inf_{\check{\tau}_p \in \mathcal{P}^{p-1}(\check{K})} \|\check{\sigma} - \check{\tau}_p\|_{H^r(\check{K})} \leq Ch^{-1/2} |\check{\sigma}|_{H^r(\check{K})} \leq Ch^r |\sigma|_{H^r(K)}.$$

For $r = p$ we obtain the expected p -rate of convergence in presence of no limitations coming from the regularity of the solution.

Let $\mathcal{P}_d^{p-1}(\partial K)$ be the space of discontinuous polynomials of degree $p-1$ defined (face by face) on ∂K . The $H(\operatorname{div})$ -interpolation result leads immediately to the best approximation error estimate in the minimum energy extension norm $H^{-1/2}(\partial K)$,

$$\inf_{t_p \in \mathcal{P}_d^{p-1}(\partial K)} \|\sigma \cdot n - t_p\|_{H^{-1/2}(\partial K)} \leq \|\sigma - \Pi\sigma\|_{H(\operatorname{div}, K)} \leq Ch^p |\sigma|_{H^p(K)}. \quad (6.34)$$

6.3 L^2 Projection Error Estimate

The standard scaling and Bramble-Hilbert arguments lead to the estimate,

$$\inf_{v_p \in \mathcal{P}^{p-1}(K)} \|u - v_p\|_{L^2(K)} \leq Ch^p |u|_{H^p(K)}. \quad (6.35)$$

7 A Priori Error Estimates

7.1 A Priori Error Estimates for the Ideal Fractional DPG Method

Polyhedra with triangular or quadrilateral faces. We recall first the standard way to approximate the best approximation error for traces in the minimum energy extension norms under the assumption that trace \hat{u} is discretized with trace \hat{w}_h of standard, H^1 -conforming finite element function w_h . We have for the $H^{1/2}$ -traces,

$$\begin{aligned} \inf_{\hat{w}_h} \|u - \hat{w}_h\|_{H^{1/2}(\partial K)} &\leq \|u - w_h\|_{H^1(K)} && \text{(definition of minimum energy extension norm)} \\ &\leq \|u - \Pi_h^{\text{grad}} u\|_{H^1(K)} \\ &\leq Ch^p \|u\|_{H^{p+1}(K)}, \end{aligned}$$

with C independent of element K and function u .

A similar argument holds for the $H^{-1/2}$ normal trace,

$$\begin{aligned} \inf_{\hat{t}_h} \|\sigma \cdot n - \hat{t}_h\|_{H^{-1/2}(\partial K)} &\leq \|\sigma - v_h\|_{H(\text{div}, K)} && \text{(definition of minimum energy extension norm)} \\ &\leq \|\sigma - \Pi_h^{\text{div}} \sigma\|_{H(\text{div}, K)} \\ &\leq Ch^p \|\sigma\|_{H^p(\text{div}, K)} \\ &\leq Ch^p \|u\|_{H^{p+1}(K)}. \end{aligned}$$

The argument extends easily from a standard element to a polyhedron with triangular or quadrilateral faces under the assumption that the polyhedron can be meshed with a submesh consisting of standard *shape regular* subelements.

Stability estimates (4.27) and (4.28) lead directly to the a-priori error estimates for the ideal DPG method:

$$\begin{aligned} &\{\gamma \|u - u_h\|_{H^{-\epsilon}(\Omega)}, (1 + C\gamma^{-1}h^{-\epsilon})^{-1} \left(\sum_{K \in \mathcal{T}_h} \{ \|\sigma \cdot n - \hat{\sigma}_{n,h}\|_{(H^{1/2-\epsilon}(\partial K))'}^2 + \|u - \hat{u}_h\|_{(H^{-1/2-\epsilon}(\partial K))'}^2 \} \right)^{\frac{1}{2}} \} \\ &\leq Ch^{-\epsilon} \inf_{w_h} \|u - w_h\|_{H^{-\epsilon}(\Omega)} + \left(\sum_{K \in \mathcal{T}_h} \{ \inf_{\hat{t}_h} \|\sigma \cdot n - \hat{t}_h\|_{H^{-1/2-\epsilon}(\partial K)}^2 + \inf_{\hat{w}_h} \|u - \hat{w}_h\|_{H^{1/2-\epsilon}(\partial K)}^2 \} \right)^{\frac{1}{2}} \\ &\leq Ch^{p-\epsilon} \|u\|_{H^{p+1}(\Omega)} \end{aligned} \tag{7.36}$$

with constants C independent of ϵ .

Polyhedra with general polygonal faces. As above, we estimate the $H^{-\epsilon}$ error with the L^2 -error, and the minimum energy extension $H^{-1/2-\epsilon}$ error with the minimum energy extension $H^{-1/2}$ error. The best approximation error estimates (6.31), (6.34), and (6.35) lead to the final estimate:

$$\begin{aligned}
& \{\gamma \|u - u_h\|_{H^{-\epsilon}(\Omega)}, (1 + C\gamma^{-1}h^{-\epsilon})^{-1} \left(\sum_{K \in \mathcal{T}_h} \{ \|\sigma \cdot n - \hat{\sigma}_{n,h}\|_{(H^{1/2-\epsilon}(\partial K))'}^2 + \|u - \hat{u}_h\|_{(H^{-1/2-\epsilon}(\partial K))'}^2 \} \right)^{\frac{1}{2}} \} \\
& \leq Ch^{-\epsilon} \inf_{w_h} \|u - w_h\|_{H^{-\epsilon}(\Omega)} + \left(\sum_{K \in \mathcal{T}_h} \{ \inf_{\hat{t}_h} \|\sigma \cdot n - \hat{t}_h\|_{H^{-1/2-\epsilon}(\partial K)}^2 + \inf_{\hat{w}_h} \|u - \hat{w}_h\|_{H^{1/2-\epsilon}(\partial K)}^2 \} \right)^{\frac{1}{2}} \\
& \leq Ch^{p-\epsilon} \|u\|_{H^{p+1}(\Omega)} + C(\epsilon) h^{p+\frac{1}{2}-\epsilon} \left(\sum_F \|u\|_{H^{p+1}(F)}^2 \right)^{\frac{1}{2}}
\end{aligned} \tag{7.37}$$

The best approximation error estimate includes a blow up constant $C(\epsilon)$ but, in presence of regular solution, the extra compensating $1/2$ convergence rate factor as well.

7.2 A Priori Error Estimates for the Practical Non-conforming DPG Method in Fractional Norms

We restrict ourselves to the polyhedral meshes only. Theorem 4 and the best approximation error estimates (6.31), (6.34), and (6.35) lead to the final estimates:

$$\begin{aligned}
& \|u - u_h\|_{H^{-\epsilon}(\Omega)} \leq \\
& C(\epsilon) h^{-3\epsilon} \left\{ Ch^{p-\epsilon} \|u\|_{H^{p+1}(\Omega)} + C(\epsilon) h^{p+\frac{1}{2}-\epsilon} \left(\sum_F \|u\|_{H^{p+1}(F)}^2 \right)^{\frac{1}{2}} \right\} \\
& \left(\sum_{K \in \mathcal{T}_h} \{ \|\sigma \cdot n - \hat{\sigma}_{n,h}\|_{(H^{1/2+\epsilon}(\partial K))'}^2 + \|u - \hat{u}_h\|_{(H^{-1/2+\epsilon}(\partial K))'}^2 \} \right)^{\frac{1}{2}} \\
& \leq C(\epsilon) h^{-4\epsilon} \left\{ Ch^{p-\epsilon} \|u\|_{H^{p+1}(\Omega)} + C(\epsilon) h^{p+\frac{1}{2}-\epsilon} \left(\sum_F \|u\|_{H^{p+1}(F)}^2 \right)^{\frac{1}{2}} \right\}.
\end{aligned} \tag{7.38}$$

There are two blow up constants above, both denoted with the same symbol $C(\epsilon)$. The first one comes from the construction of the Fortin operator which is invalid in the limit $\epsilon = 0$, the second one from the localization argument in the best approximation minimum energy extension $H^{1/2-\epsilon}$ error estimate.

8 Numerical Experiments

8.1 About the implementation

This section exclusively considers the three-dimensional case ($N = 3$). A modified version of the hp -adaptive finite element code *hp3D* by Demkowicz et al. (see [28]) has been implemented in order to support high-order approximation with (simple) polyhedral elements of arbitrary number of vertices and (flat) faces. The new code is able to obtain the practical DPG solution of any well-posed broken ultraweak variational formulation, but with discontinuous discrete traces. However, when all faces in the mesh skeleton are triangular, the code can enforce continuity of the traces if wanted.

This PolyDPG code uses the Nédélec spaces of the first kind for tetrahedra for the element variables (fields), and those of the triangle for the face variables (traces). The details are presented below.

8.1.1 Discrete trial spaces

For any positive polynomial degree p , the discrete trial functions $\mathbf{u}_h = (\sigma_h, u_h, \hat{\sigma}_{n,h}, \hat{u}_h)$ correspond to the following spaces:

$$\begin{aligned}\sigma_h &\in \{q_h \in (L^2(\Omega))^N : q_h|_K \in (\mathcal{P}^{p-1}(K))^N \text{ for every } K \in \mathcal{T}_h\}; \\ u_h &\in \{w_h \in L^2(\Omega) : w_h|_K \in \mathcal{P}^{p-1}(K) \text{ for every } K \in \mathcal{T}_h\}; \\ \hat{\sigma}_{n,h} &\in \{\hat{q}_h \in H^{-1/2}(\Gamma_h) : \hat{q}_h|_F \in \mathcal{P}^{p-1}(F) \text{ for every face } F \subset \Gamma_h\}; \\ \hat{u}_h &\in \{\hat{w}_h \in L^2(\Gamma_h) : \hat{w}_h|_F \in \mathcal{P}^p(F) \text{ for every face } F \subset \Gamma_h\}.\end{aligned}$$

8.1.2 Broken test spaces

The enriched test spaces that we employ for the practical DPG method are also formed by piecewise polynomials of degree higher than that of the trial space. To have a sufficiently enriched local test space we propose two strategies.

First option: p -enrichment. Let $\delta p(K)$ be a positive integer possibly depending on element K such that the local test space consists of polynomials of order less than or equal to $p + \delta p(K)$. This enrichment parameter may be chosen to be constant throughout the mesh, or variable. The enriched test functions $\mathbf{v} = (\tau, v)$ belong to the following spaces:

$$\begin{aligned}\tau &\in \{\mathbf{q} \in H(\text{div}, \mathcal{T}_h) : \mathbf{q}|_K \in \mathcal{RT}^{p+\delta p(K)}(K) \text{ for every } K \in \mathcal{T}_h\}; \\ v &\in \{w \in H^1(\mathcal{T}_h) : w|_K \in \mathcal{P}^{p+\delta p(K)}(K) \text{ for every } K \in \mathcal{T}_h\}.\end{aligned}$$

The space \mathcal{RT}^r is the $H(\text{div})$ -conforming (Raviart-Thomas-like) space of order r . It is usually intended that the dimension of the resulting local test space be larger than the dimension of the local trial space. For polyhedral elements with many faces, this may result in a high δp because the number of local traces grows proportionally to the number of faces.

Second option: hp -enrichment. For each element $K \in \mathcal{T}_h$ we assume that a shape-regular tetrahedral subtessellation $\mathcal{S}(K)$ can be constructed. Then we can construct a conforming subspace of $H(\text{div}, K) \times$

$H^1(K)$ using the subtessellation. The local test functions and their spaces are therefore:

$$\begin{aligned}\tau|_K &\in \left\{ \mathbf{q} \in H(\operatorname{div}, K) : \mathbf{q}|_T \in \mathcal{RT}^{p+\delta p(K)}(T) \text{ for every } T \in \mathcal{S}(K) \right\}; \\ v|_K &\in \left\{ w \in H^1(K) : w|_T \in \mathcal{P}^{p+\delta p(K)}(T) \text{ for every } T \in \mathcal{S}(K) \right\}.\end{aligned}$$

The larger the number of faces and vertices in an element, the larger the number of tetrahedra in the subtessellation becomes. This turns out to be an effective way of enriching the test space, since usually even with a low δp the dimension of the test space is considerably bigger than that of the local trial space. It is shown in [36] that $\delta p = 2$ implies the existence of a Fortin operator for the non-conforming DPG for tetrahedra. Using the ideas given in Appendix A this result can be extended to the subtessellation, but in most cases reported below the convergence is obtained even with $\delta p = 1$. This means that this strategy facilitates the application of PolyDPG with a higher order of approximation, provided there is an efficient method to generate uniform shape-regular submeshes.

8.1.3 Bases and integration

For the first test space option, the integration of the local Gram and stiffness matrices is carried out using the so called *homogeneous numerical integration (HNI)*, which needs homogeneous integrands to transform volume integrals into boundary integrals for any convex or non-convex polyhedron [39, 42, 18]. To take advantage of this technique, the bases of our element polynomial spaces are made of monomials. However, when integrating the load vector or the error, the numerical integration is performed using a composite Gaussian quadrature corresponding to a tetrahedral subtessellation of the polyhedron and standard quadrature for tetrahedra.

If the second test space option is preferred, then HNI is not viable because the bases for the test functions cannot be monomials but rather conforming shape functions such as those described in [32]. The approach in this case is to compute the integrals subelement-wise, and then perform a local assembly.

8.2 Results

We restrict the numerical study to the Poisson model problem analyzed above. Although this paper derives theoretical findings for variational problems formulated in fractional Sobolev spaces, here we compute with the limit case only ($\epsilon = 0$).

For all cases we use smooth non-polynomial manufactured solutions u_{exact} and Dirichlet boundary conditions on the whole boundary. To obtain the rest of the exact solution components we calculate $\sigma_{exact} = \nabla u_{exact}$ and get the traces $(\hat{u}_{exact}, \hat{\sigma}_{n,exact})$ by simple restriction on every face of the mesh skeleton. The boundary condition is given by $\hat{u}_{exact}|_{\partial\Omega}$. Finally, the right-hand side load is determined by $f = -\Delta u_{exact}$.

The norms used to evaluate the error are:

$$\begin{aligned} \text{Error in } u_h &= \frac{\|u - u_h\|_{L^2(\Omega)}}{\|u_{exact}\|_{L^2(\Omega)}}. \\ \text{Error in } \sigma_h &= \frac{\|\sigma_{exact} - \sigma_h\|_{L^2(\Omega)}}{\|\sigma_{exact}\|_{L^2(\Omega)}}. \\ \text{Error in } \hat{u}_h &= \left(\sum_{\text{Face } F \subset \partial\mathcal{T}} h_F^{-1} \|\hat{u}_{exact} - \hat{u}_h\|_{L^2(F)}^2 \right)^{1/2}. \\ \text{Error in } \hat{\sigma}_{n,h} &= \left(\sum_{\text{Face } F \subset \partial\mathcal{T}} h_F \|\hat{\sigma}_{n,exact} - \hat{\sigma}_{n,h}\|_{L^2(F)}^2 \right)^{1/2}. \end{aligned}$$

Observe that the first two deliver relative errors, while the other two give absolute errors as they are mesh-dependent norms. The choice of such error metrics for the traces is mainly driven by the need of having a cheap way to evaluate it. Both trace norms scale in element size h in the same way as the actual fractional norms.

In the following error convergence graphs, instead of considering the mesh size parameter h , we use the total number of degrees of freedom (DOF), because if we use a quasiuniform mesh we can assert that $h^{-3} \sim \text{Total DOF}$.

We present three sets of results, which let us explore the flexibility of the DPG methodology with non-conforming traces and polyhedral elements. First, we use structured meshes with four different element sizes and observe the numerical convergence for low and high order approximations. Second, we go for a more general polyhedral mesh, namely a Voronoi tessellation, and even with such irregular elements we see how the numerical solution improves with a finer mesh and a higher polynomial degree. The third result set is motivated by a more practical point of view. There, we first use a popular tetrahedral mesh generator, which delivers unstructured meshes for certain domain. In addition to using the simplicial partition per se, we also use the idea of element agglomeration (or aggregation) [2, 20] in order to obtain polyhedral elements. Moreover, we use the fact that all faces are triangular to construct globally continuous trace spaces. We can therefore compare the behavior of such meshes with both continuous and discontinuous traces (whether with or without agglomeration). The practicality lies in two facts: i) by agglomerating portions of a fine mesh, we reduce the number of degrees of freedom while keeping the detailed representation of the geometry; ii) the underlying submesh provides a shape-regular partition as the one we assume in our theoretical setting, and can be used for integration, visualization, and adaptive refinement or coarsening. Although adaptivity is beyond the scope of the present publication, it is a subject of interest for future research on DPG with polyhedral elements.

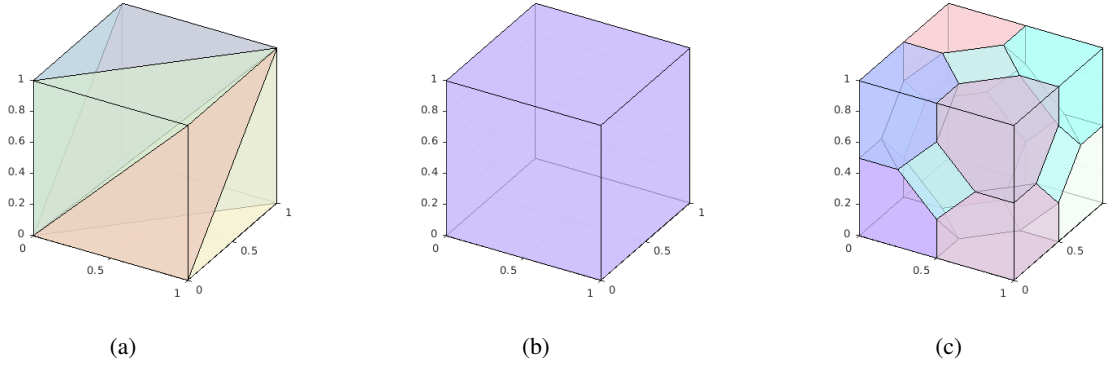


Figure 8.1: Coarse meshes for the first numerical study: (a) tetrahedra (6 elements), (b) cubes (1 element), (c) truncated octahedra (9 elements).

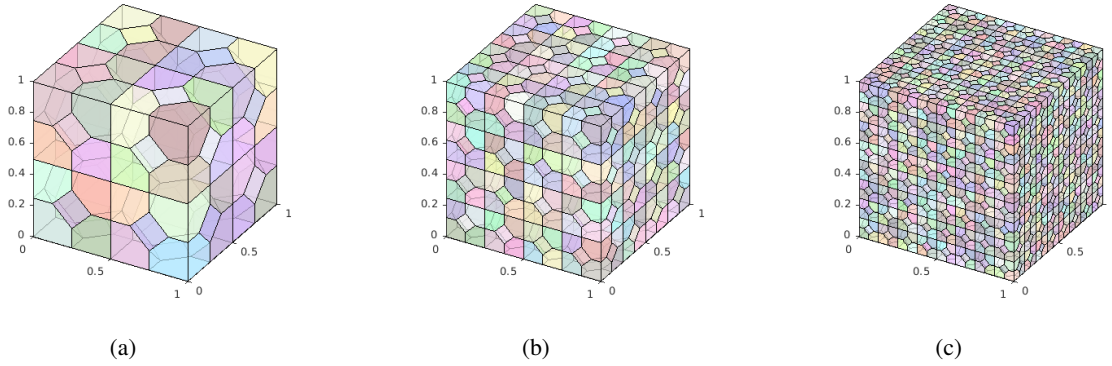


Figure 8.2: Fine truncated-octahedral meshes for the first numerical study: (a) 72 elements, (b) 576 elements, (c) 4608 elements.

8.2.1 Results with structured meshes

Our first domain is $\Omega = (0, 1)^3$ and the manufactured solution is

$$u_{exact}(x) = \exp(x_1 + x_2 + x_3).$$

Notice that the gradient of $u_{exact}(x)$ consists of three copies of $\exp(x_1 + x_2 + x_3)$ and that the load is $f(x) = -3 \exp(x_1 + x_2 + x_3)$.

Three families of meshes consisting of structured tetrahedra, cubes and truncated octahedra are utilized. The coarsest meshes considered in this initial example are presented in Figure 8.1. Each of those is reproduced 8 times and scaled down to a half its size. This process is repeated 3 times, so that we have four meshes in each family. The refined meshes made with truncated octahedra can be visualized in Figure 8.2. Notice that these polyhedral elements have 7 and 14 faces, including pentagonal and hexagonal faces.

For each mesh, we use polynomial orders $p = 1, 2, 3, 4$. However, the enrichment parameter δp must vary according to the type of element, intuitively requiring a higher enrichment as the number of faces

increases. In this first problem we only use the p -enrichment option. Sample solution plots are shown in Figure 8.3, where the type of mesh, order of approximation and enrichment parameter are reported. Using

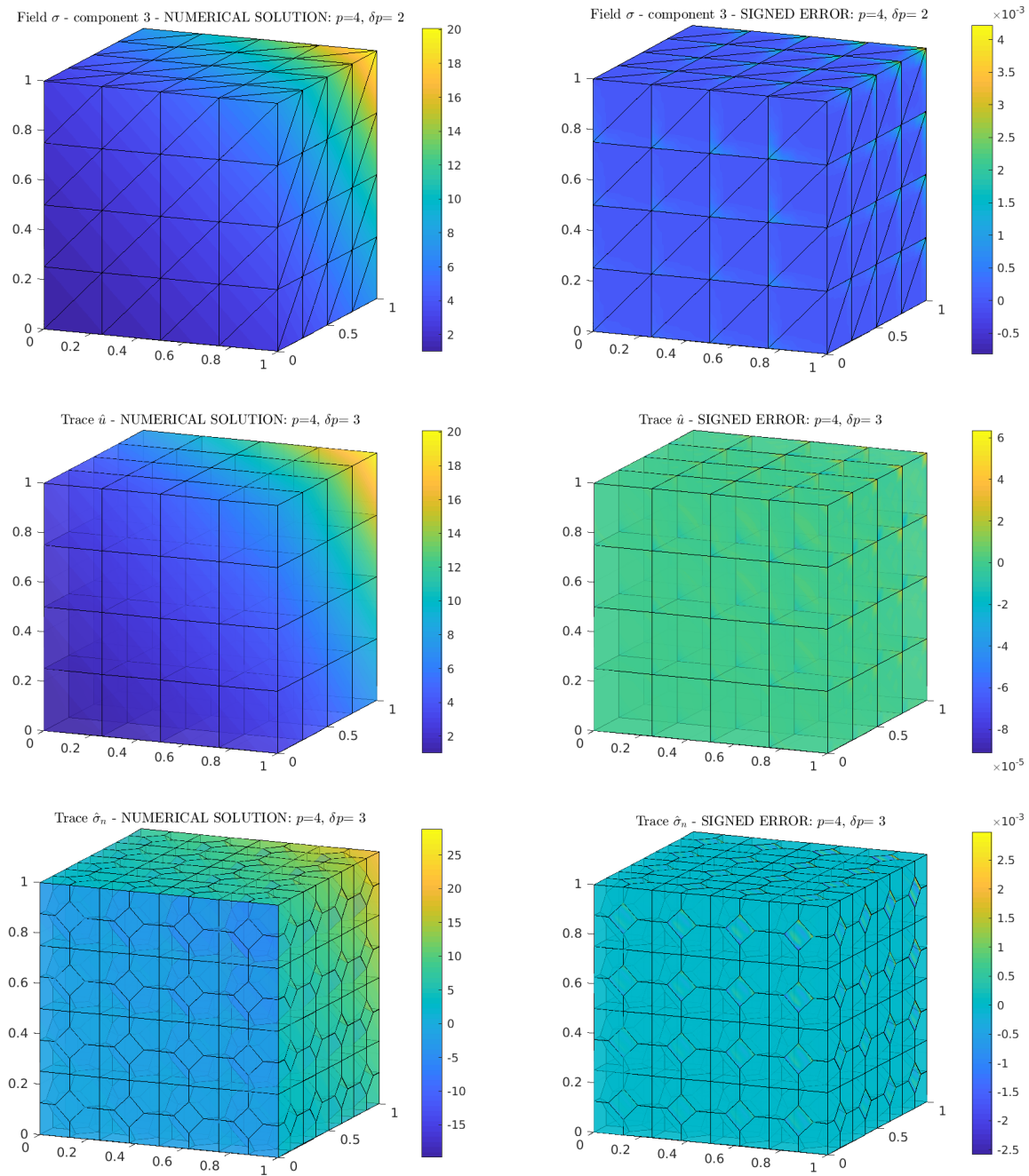


Figure 8.3: Sample plots of pointwise numerical solution (left) and signed error (right): (top) field variable $(\sigma_h)_3$ in a mesh of 384 tetrahedra, with $p = 4$ and constant $\delta p = 2$; (middle) trace variable \hat{u}_h in a mesh of 64 cubes, with $p = 4$ and constant $\delta p = 3$; (bottom) trace variable $\hat{\sigma}_{n,h}$ in a mesh of 576 truncated octahedra, with $p = 4$ and constant $\delta p = 3$.

the error metrics given above, we plot the numerical error convergence for the three mesh families in Figures 8.4, 8.5 and 8.6. It is clear how the convergence is attained in all the mesh families and with the expected rates, for all the unknowns of the broken ultraweak formulation. Having such results, it can be said that for these types of polyhedral meshes it is a good choice to utilize p -enrichment because it enables a fast computation thanks to the HNI quadrature.

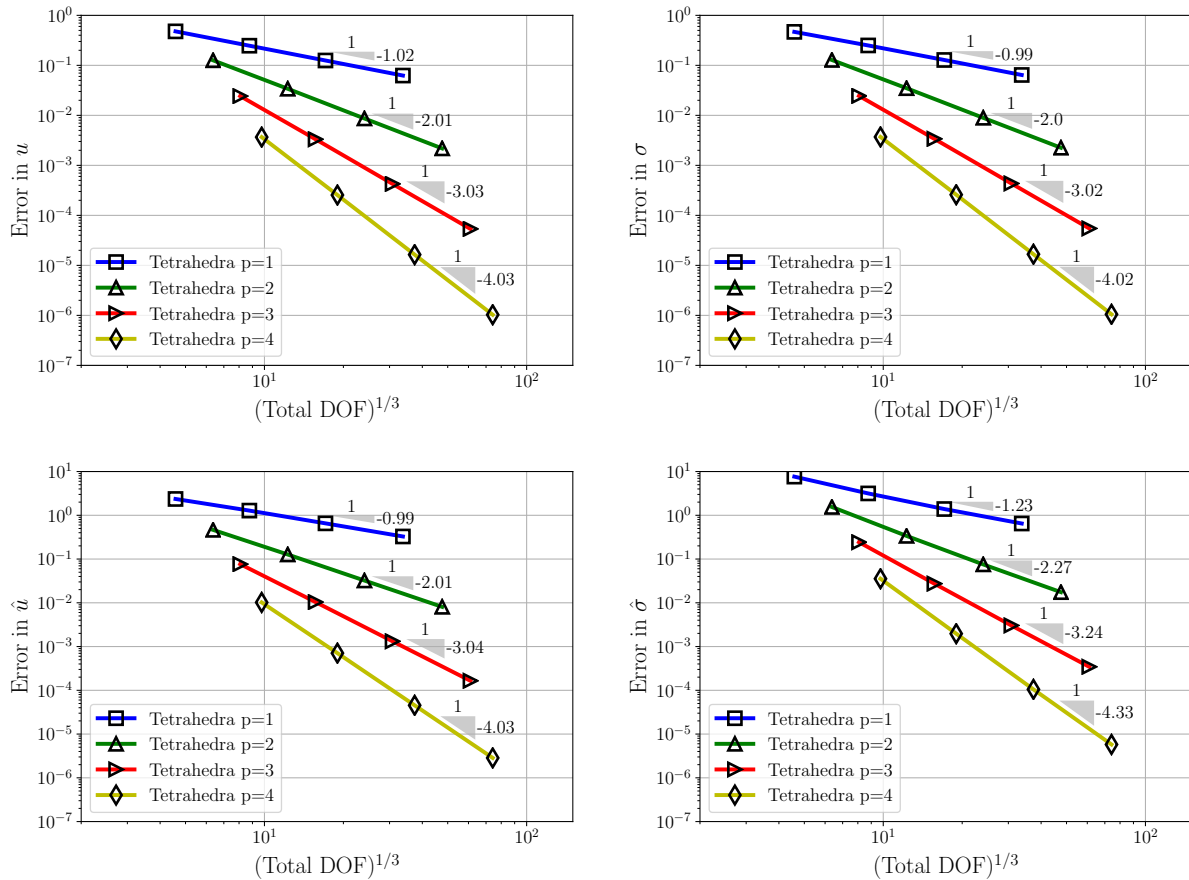


Figure 8.4: Error convergence in all variables for the tetrahedral mesh family and four polynomial orders. The constant p -enrichment parameter is $\delta p = 2$.

8.2.2 Results with Voronoi cells

For the second scenario we change the domain for $\Omega = (-1/2, 1/2)^3$ and keep the same manufactured solution. The meshes to be considered in this second study are generated through an algorithm called VoroCrust, which generates boundary-conforming Voronoi tessellations without clipping, even for complex 3D geometries (sharp features, multiple boundary components, non-watertight or non-manifold surfaces, etc.) [1].

In our current case we present meshes for the cube Ω , but as a result of VoroCrust, each element in the

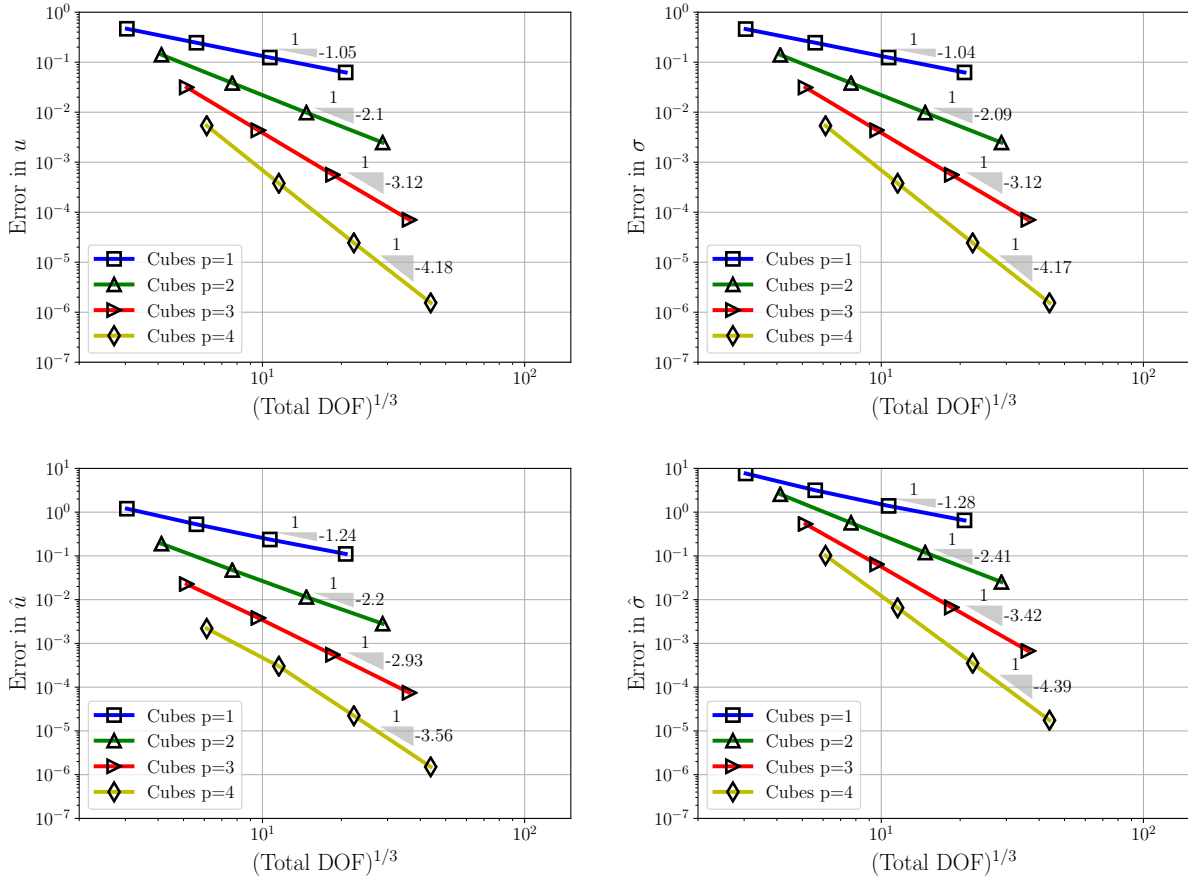


Figure 8.5: Error convergence in all variables for the cubic mesh family and four polynomial orders. The constant p -enrichment parameter is $\delta p = 3$.

mesh is a real Voronoi cell, and all faces lying on the domain boundary are triangles. Because of the random sampling used in the meshing algorithm herein used, the cells in the partition may have a large number of neighbors (i.e., of faces). In Figure 8.7 we can visualize the exterior of a VoroCrust mesh and show the aspect of its interior elements. Some of those elements present over 40 faces, a feature that will demand a very high test space enrichment. Here, we report results of computations of our method over three different VoroCrust meshes, which consist of 204, 560 and 1650 elements.

Polynomial orders $p = 1, 2, 3$ are used with the Voronoi meshes, and both test enrichment options are applied. For the first option, the constant p -enrichment parameter is $\delta p = 6$ in most cases, although for $p = 3$ the highest enrichment that we can compute with is $\delta p = 5$. Regarding the hp -enrichment option, we construct the local test spaces with tetrahedral submeshes generated on the fly, and $\delta p = 1$. Because the latter parameter is not as high as in the p -enrichment case, we can even compute with higher order ($p = 4$ is added for this option). Unfortunately, the shape-regularity of these submeshes is not guaranteed due to the simplicity of the method with which these are constructed.

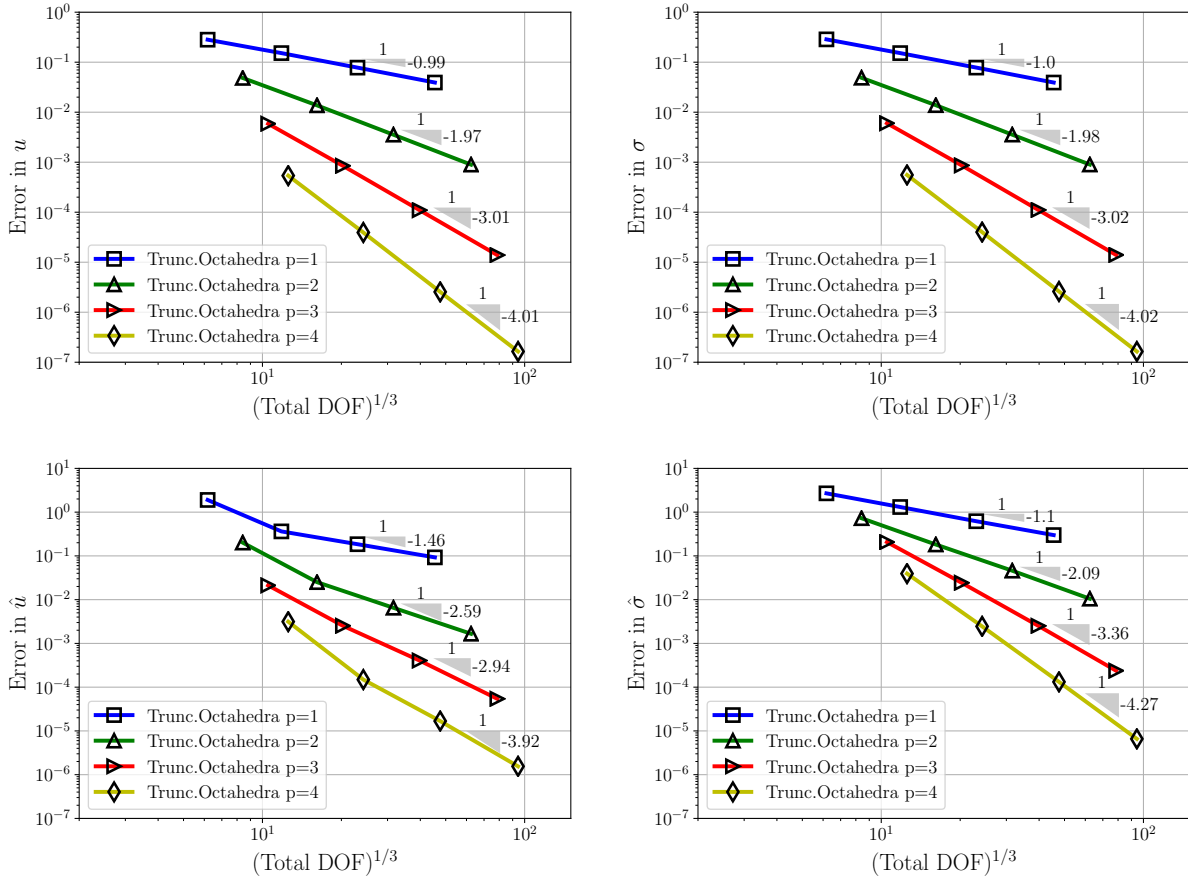


Figure 8.6: Error convergence in all variables for the truncated-octahedral mesh family and four polynomial orders. The constant p -enrichment parameter is $\delta p = 3$.

Figure 8.8 includes sample plots of the numerical solution and error of one field variable, along with cut views of the resulting scalar field u_h . On this plane, the solution should be constant, so we see how the approximation improves when passing from the lowest order case to $p = 2$. It is worth mentioning that the solution of the field variables u_h and σ_h is virtually equal for either test enrichment option, but the results for the traces are largely distinct. More precisely, variables \hat{u}_h and $\hat{\sigma}_{n,h}$ diverge when using the p -enrichment option. Finally, in Figures 8.9 and 8.10 we show the error convergence graphs corresponding to the p - and hp -enrichment options, respectively (traces for the first enrichment option are omitted). Notice that the observed rates are close to the theoretical ones in all the cases therein included, although they slightly deteriorate as p increases.

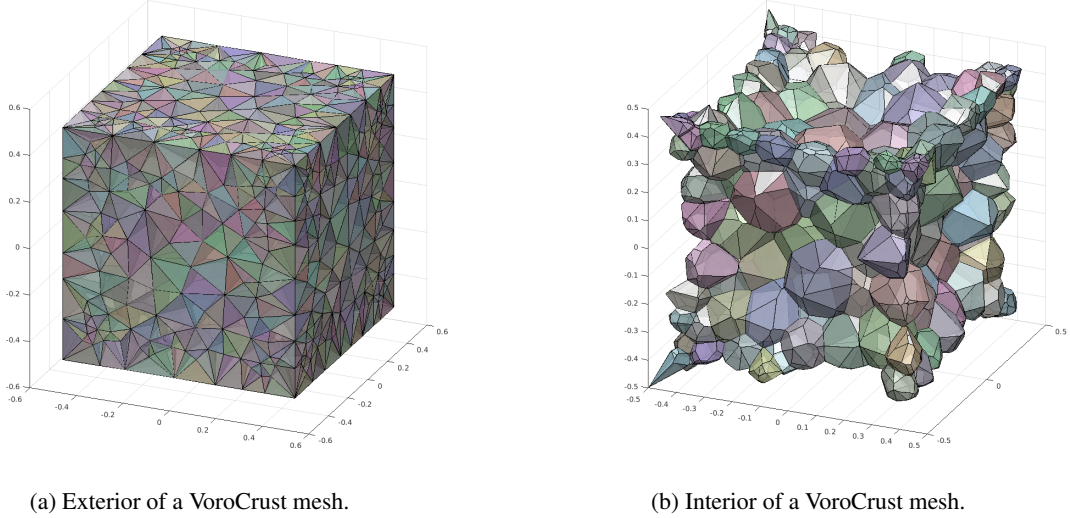


Figure 8.7: Polyhedral mesh generated with VoroCrust.

8.2.3 Results with unstructured tetrahedral meshes

The third setup uses another manufactured solution,

$$u_{exact}(x) = \sin(\pi x_1) \sin(\pi x_2) \sin(\pi x_3).$$

As for the domain herein used, we have again $\Omega = (-1/2, 1/2)^3$, but including an interface between two subdomains: a sphere of radius $1/4$ and centered at the origin, and its complement in Ω . This is depicted in Figure 8.11(a). There is consequently a spherical surface that must be conformingly meshed. Even though we are not assigning different material properties to the subdomains, studying this geometric configuration will be of importance in many practical applications modelled with PDEs less simple than the Poisson equation. This geometry is meshed with NETGEN, a well-established unstructured tetrahedral mesh generator (<https://ngsolve.org/>). Three meshes of 1545, 9462 and 27066 tetrahedra are obtained with this tool. The second of them can be appreciated in Figure 8.11(b),(c).

We run our method on these meshes for polynomial orders $p = 3, 4, 5$ and the p -enrichment option only. Sample plots of the numerical solution of both skeleton variables are presented in Figure 8.12.

Continuous traces. Due to all faces being triangular, we can construct a globally continuous trace space for \hat{u}_h . For its implementation, we just need to know the relative orientation of edges with respect to faces to perform a modified assembly. However, all operations at the element level remain identical to the former procedure, save for a more careful evaluation of the face shape functions, as the orientations must be taken into account. For the meshes at hand, the enforcement of continuity of the trace makes this method a conforming finite element discretization, in the context of the broken ultraweak formulation. It can be regarded then as a conventional DPG discretization.

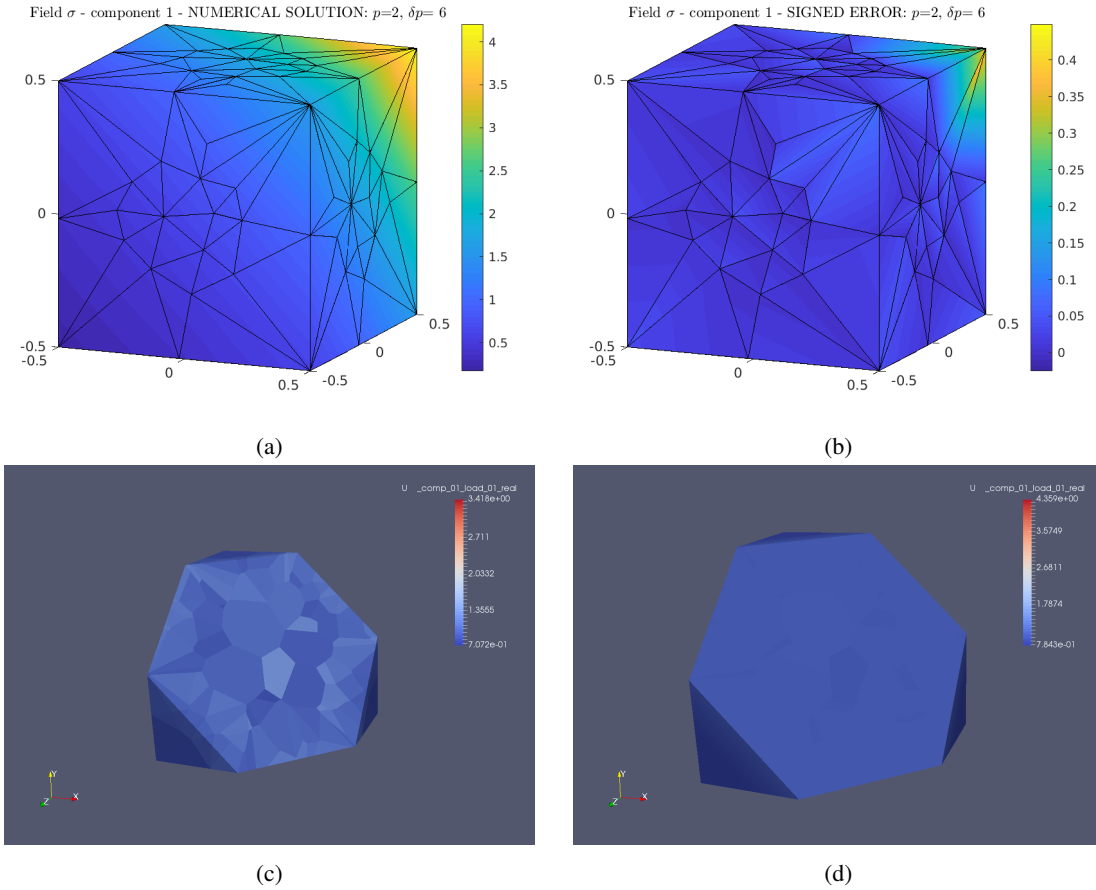


Figure 8.8: Sample plots of pointwise numerical results with Voronoi meshes using p -enrichment: (a) solution for field variable $(\sigma_h)_1$ in the 204-element Voronoi mesh with $p = 2$, constant $\delta p = 6$; (b) signed error for field variable $(\sigma_h)_1$ in the 204-element Voronoi mesh with $p = 2$, constant $\delta p = 6$; (c) solution for field variable u_h in a cut view of the 560-element Voronoi mesh with $p = 1$, constant $\delta p = 6$; (d) solution for field variable u_h in a cut view of the 560-element Voronoi mesh with $p = 2$, $\delta p = 6$.

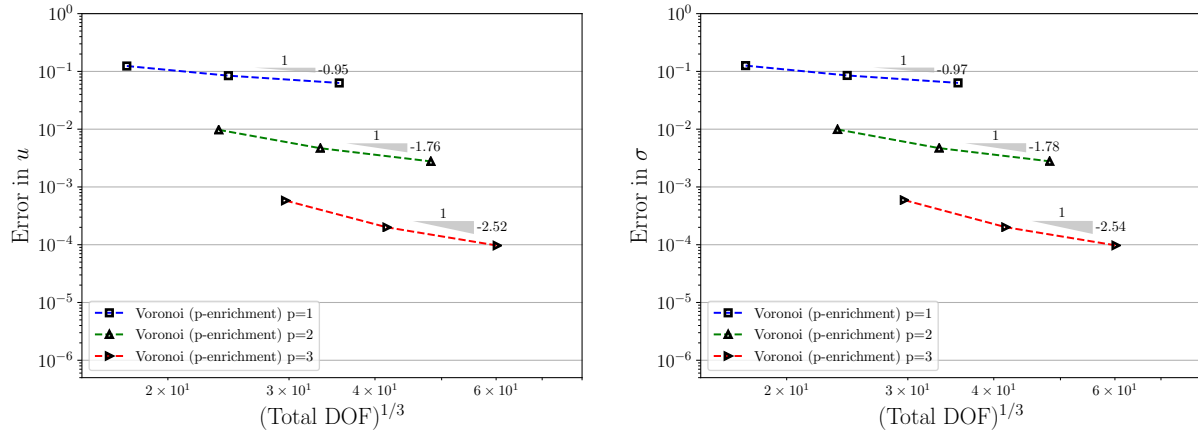


Figure 8.9: Error convergence in the field variables for the Voronoi mesh family and three polynomial orders, using p -enrichment.

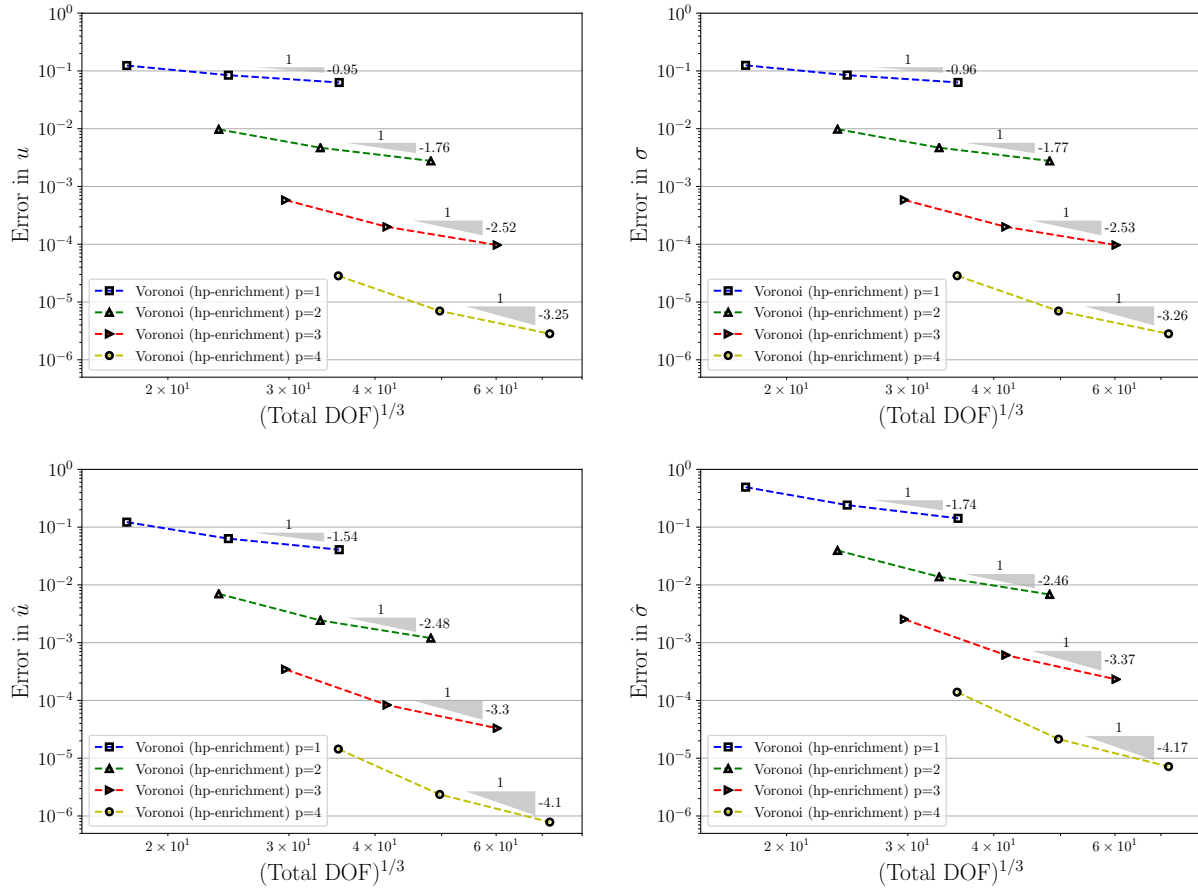


Figure 8.10: Error convergence in all variables for the Voronoi mesh family and four polynomial orders, using hp -enrichment.

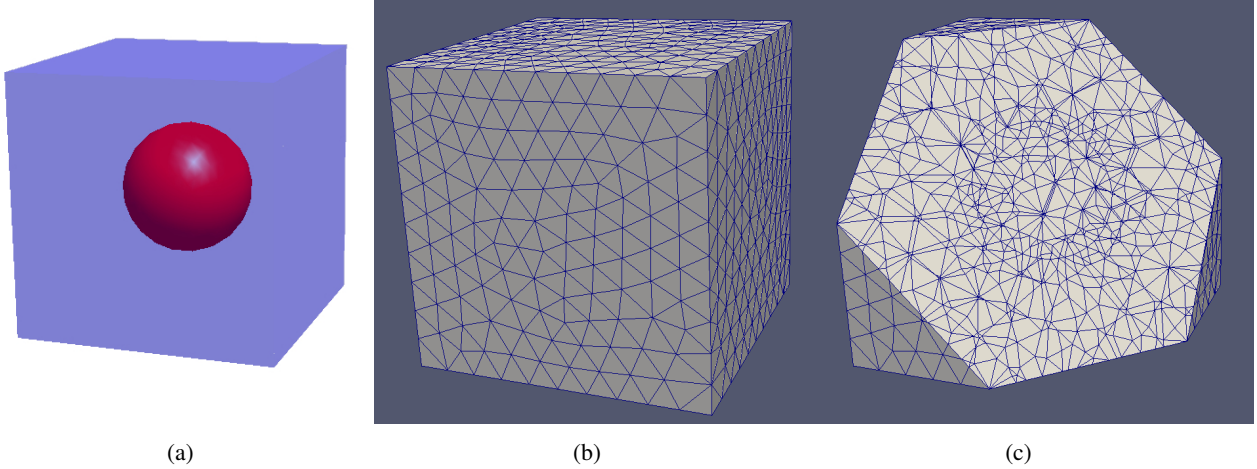


Figure 8.11: (a) The domain Ω showing an interior spherical surface that stands as the interface between two subdomains; (b) exterior of an unstructured 9462-element tetrahedral mesh of Ω ; (c) cut view of the mesh, where the conformity to the interior surface is visible.

Plots in Figure 8.13 show the same variables as above, where small differences in the error can be observed, but most importantly the continuity of the numerical approximation to \hat{u} can be visualized. Figure 8.14 show convergence of all variables with these unstructured meshes, for both the continuous and the discontinuous discretization of the trace. It can be seen how enforcing continuity only saves relatively few DOF, while the error is almost identical to the solution with discontinuous traces. Notice how the case $p = 5$ for the variable u_h initially experiences a great error decrease, but for the finest mesh, there is almost no improvement. We attribute such loss (in just 1 out of 4 unknowns) to numerical conditioning.

Element agglomeration. The implementation of the element agglomeration approach is realized with the use of the graph-partitioning library METIS [37]. In order to have agglomerated elements that belong to a single subdomain, the agglomeration process is performed on one subdomain at a time. It is possible to set the approximate number of tetrahedra per agglomeration, and here we use 16 and 64. Using this option delivers a very large number of faces per elements, since all triangles lying on the boundary of an agglomerated portion of the mesh is considered as an independent face, even if there are coplanar adjacent triangles. Unlike the above cases, the agglomerated elements may be non-convex. One of the partitions obtained by applying the agglomeration algorithm to one of the unstructured meshes above is visualized in Figure 8.15 (refer to Figure 8.11(b),(c) to identify the original elements before agglomeration).

In order to assess the performance of PolyDPG with these meshes, all three unstructured tetrahedral meshes are utilized, subject to different agglomeration densities and approximation orders. Moreover, both of the test enrichment options are applied, obtaining the results next explained.

Concerning the computations with p -enrichment it is noticeable that even though we have a large number of faces in any case, the enrichment parameter δp needs not be so high when having continuous traces in

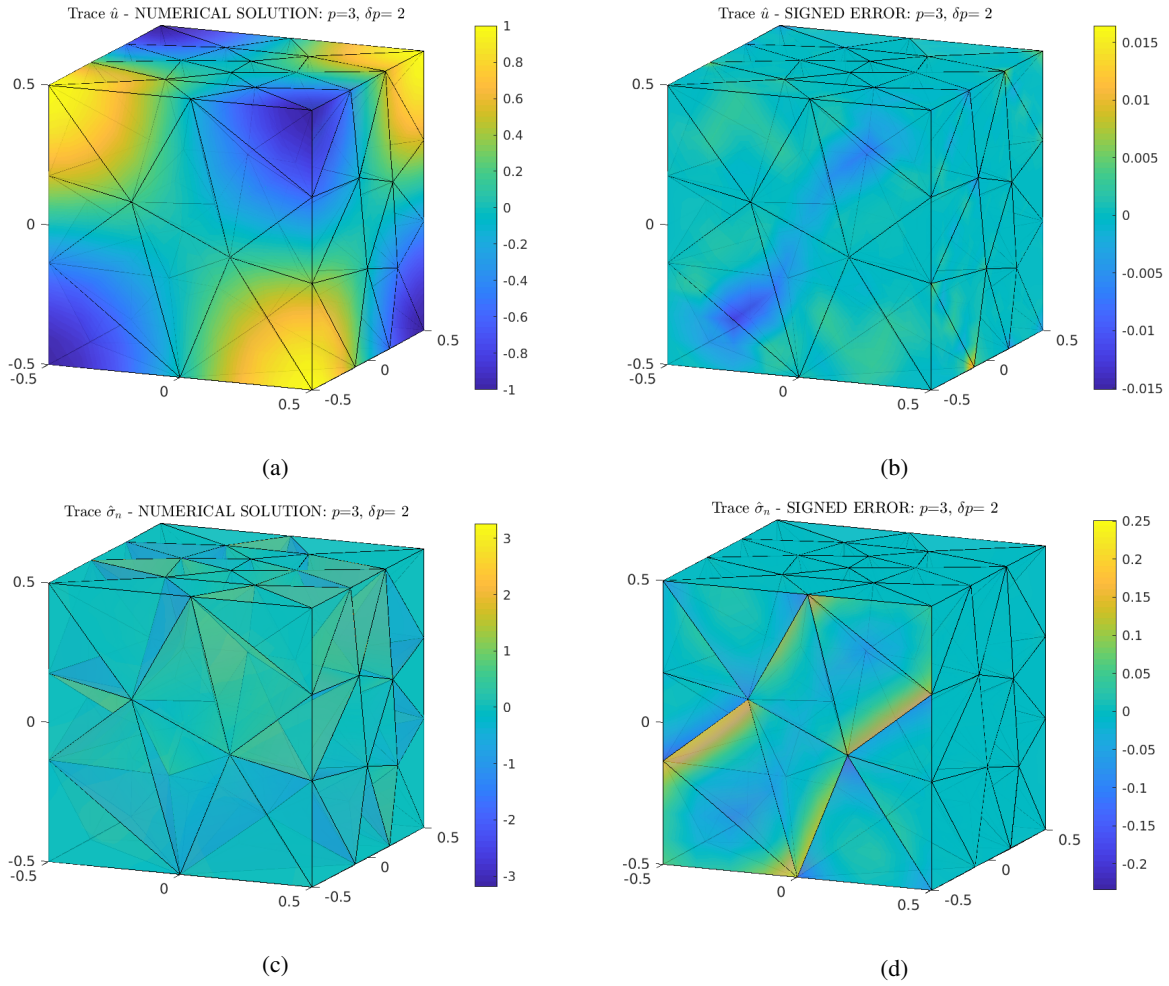


Figure 8.12: Sample plots of pointwise numerical solution (left) and signed error (right) in the 1545-element unstructured tetrahedral mesh, with $p = 3$ and $\delta p = 2$: (top) variable \hat{u}_h ; (bottom) variable $\hat{\sigma}_{n,h}$.

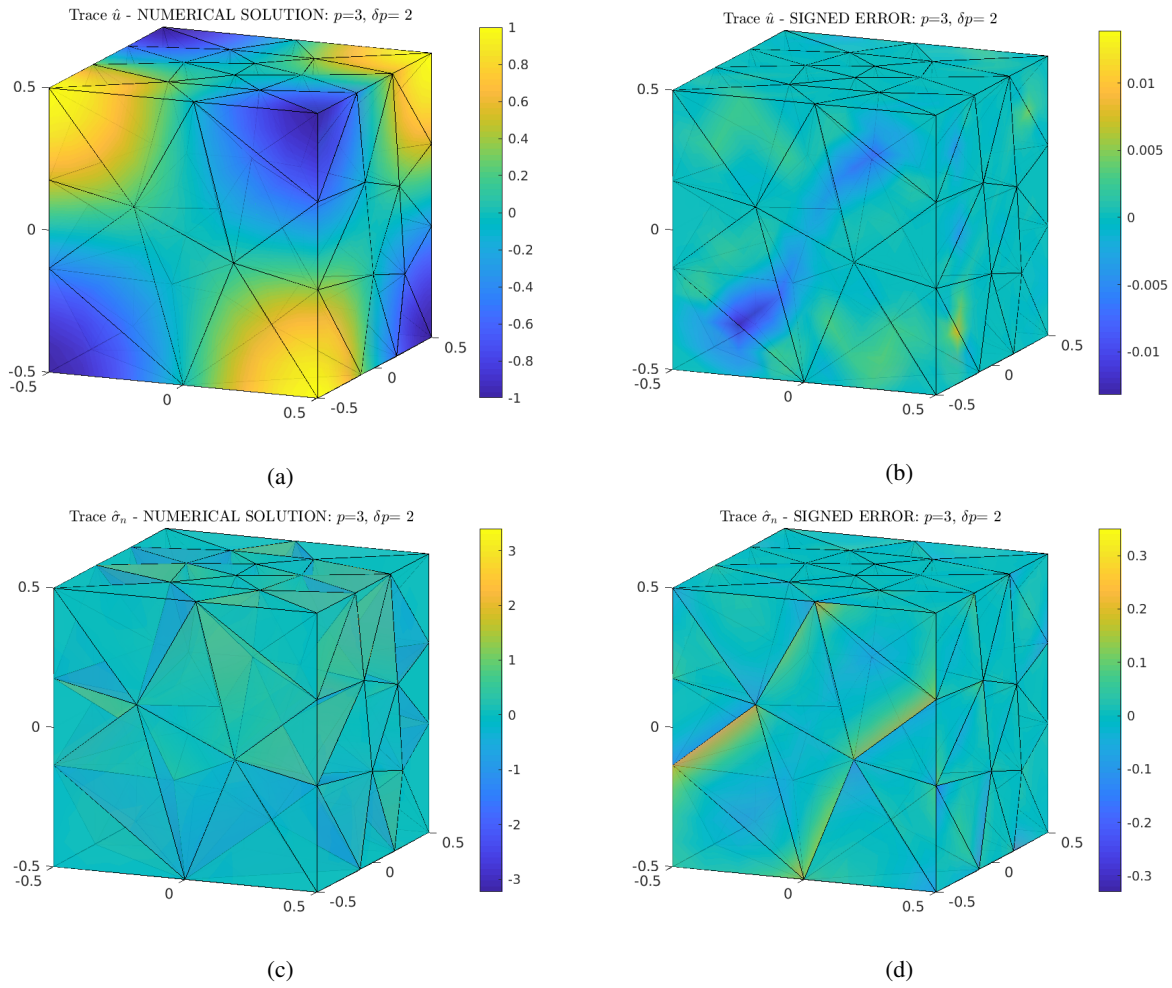


Figure 8.13: Sample plots of pointwise numerical solution (left) and signed error (right) in the 1545-element unstructured tetrahedral mesh **enforcing continuous discretization of trace \hat{u}** , with $p = 3$ and $\delta p = 2$: (top) variable \hat{u}_h ; (bottom) variable $\hat{\sigma}_{n,h}$.

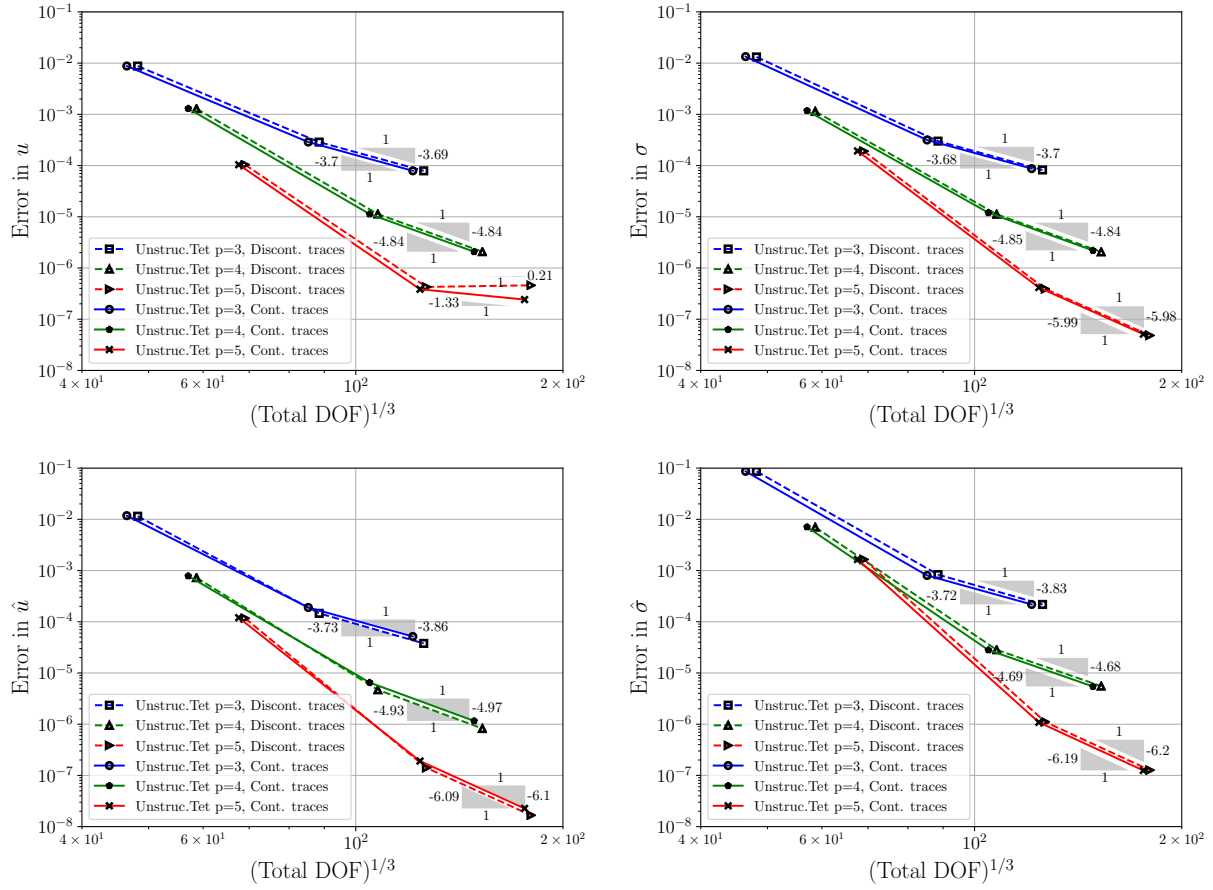


Figure 8.14: Error convergence in all variables for the unstructured tetrahedral mesh family and three polynomial orders, considering both discontinuous and continuous discretization of \hat{u} . The p -enrichment parameter is $\delta p = 2$.

order to observe convergence in most unknowns. A consequence of this is that we can raise p or agglomerate a greater quantity of tetrahedra when we enforce continuous traces. Sample plots of the numerical solution with $p = 3$ are shown in Figure 8.16 with both discontinuous and continuous traces. Error convergence graphs for three variables are given in 8.17, including both types of trace discretization. There, only for the continuous trace scenario, we add two more series of results: the case $p = 4$ in the same meshes (16 tetrahedra per element), and the case $p = 3$ on a new set of meshes with 64 tetrahedra per element. Notice that in the case $p = 4$ we observe a significant improvement with respect to the other cases, and given that the rate is higher than 4, it rapidly reaches error levels that may be good enough for a practical problem. In none of these scenarios convergence of the fourth variable is observed.

On the other hand, it is natural to try the hp -enrichment strategy, since a shape-regular submesh is already available thanks to the agglomeration process. In this case we can compute with 64 tetrahedra/element with the nonconforming discretization, getting the same convergence behavior as in the case of conforming traces. A similar result holds for the case $p = 4$, although in this case $\delta p = 2$ is necessary for the convergence of all the variables, with both continuous and discontinuous \hat{u}_h and both agglomeration densities considered. However, applying the latter $(p, \delta p)$ combination in the hp -enrichment option noticeably slows down the local computations. The error behavior in all variables for the case 16 tetrahedra/element is presented in Figure 8.18, while the corresponding to 64 tetrahedra/element is shown in Figure 8.19.

We can see in the error convergence plots for agglomerated elements that we have good rates, but because of the reduced amount of DOF, the magnitude of the error is still far from that of the original tetrahedral mesh, and the bounding constant seems to be slightly greater in the current setup.

A caveat for this approach can be observed during the solving stage, which takes much longer than with other meshes used in the current work. We attribute such a major slowdown to the high number of faces that each element possesses, having to interact with many neighbors. This implies that the final DPG stiffness matrix is way less sparse than for elements with few faces, and the performance of the MUMPS solver gets therefore affected.

9 Conclusions

We have presented a stability and convergence analysis for a class of DPG methods based on the ultraweak (UW) variational formulation for general polyhedral meshes for a model Poisson problem in 3D. The DPG methodology based on the UW formulation offers the most relaxed setting in terms of conformity. Only one variable - the $H^{1/2}$ trace, defined on the mesh skeleton, needs to be continuous in order to guarantee a fully conforming discretization based on the standard energy spaces setting. If we employ polyhedra with triangular or quadrilateral faces, construction of continuous traces is straightforward, and the standard analysis applies [52]. In the case of polyhedra with non-triangular (or non-quadrilateral) faces, the situation is different, and we are naturally led to a non-conforming discretization of traces based on discontinuous polynomials.

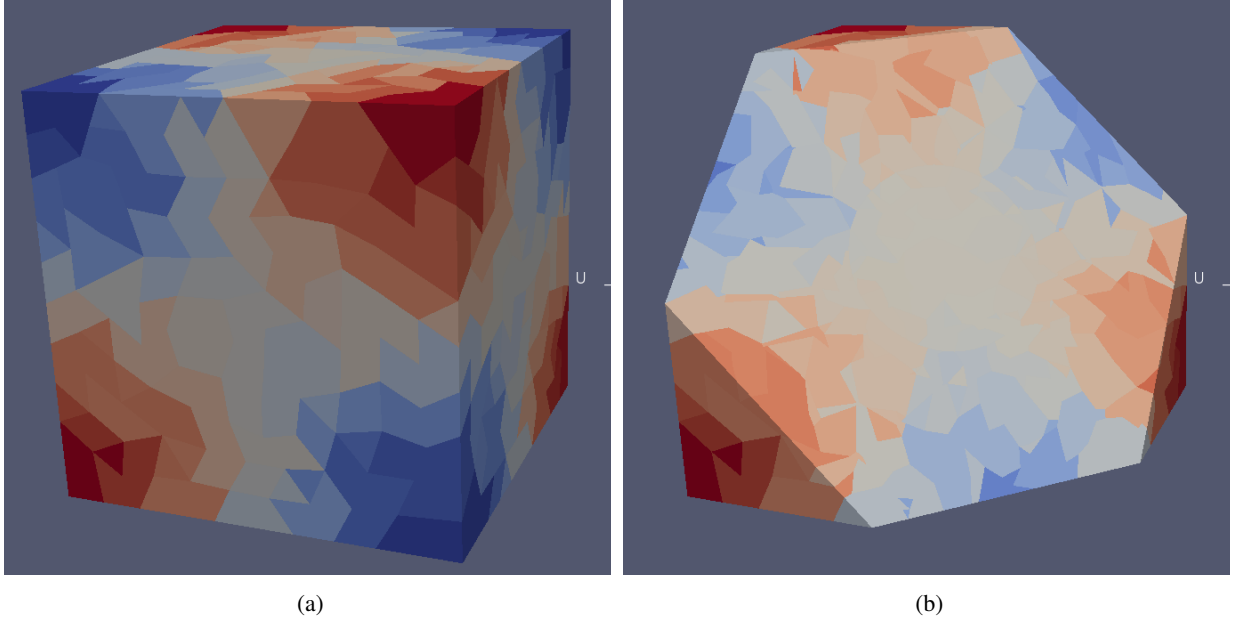


Figure 8.15: Agglomerated mesh, with about 16 tetrahedra per element: (a) exterior view, with each constant color representing a different element; (b) cut view showing that the agglomerated elements do not cross the subdomain interface.

The presented work builds on the logical construction proposed by Heuer et al. [36] who analysed the non-conforming UW DPG method on standard tetrahedral meshes. Without changing the actual computational paradigm, the authors investigate a different functional setting where the $H(\text{div})$ ‘broken’ test norm is complemented with additional L^2 boundary terms. The use of the stronger test norm results in a weaker trial norm for traces in which the discontinuous traces become conforming. The authors relate the two versions of the DPG method after the discretization of enriched test spaces (the practical DPG method) and, in the end, they are able to prove the L^2 -convergence for the original unknown.

Our modified functional setting employs fractional energy spaces with ϵ -weaker trial spaces and ϵ -stronger test spaces. In the weaker trial spaces, the discontinuous traces become conforming. We prove the well-posedness of the broken UW formulation and the stability of the corresponding ideal DPG method. This analysis stands on its own. In particular, we had to understand the behavior of equivalence constants for $\epsilon \rightarrow 0$ for as many as five different definitions of fractional Sobolev spaces.

We follow then the methodology of [36] and use the established stability in the fractional norms to prove convergence of the original non-conforming DPG method. In the end, we are able to prove the convergence for the non-conforming DPG method in the relaxed ϵ -weaker norms *for all unknowns*. Unfortunately, we have not been able to pass with ϵ to zero.

The paper contains also an extensive computational component. The numerical experiments have covered a broad set of polyhedral element shapes, mesh types, approximation orders and test enrichment options. In all cases, the convergence rate of the field variables is very close to the expected rate, whereas the

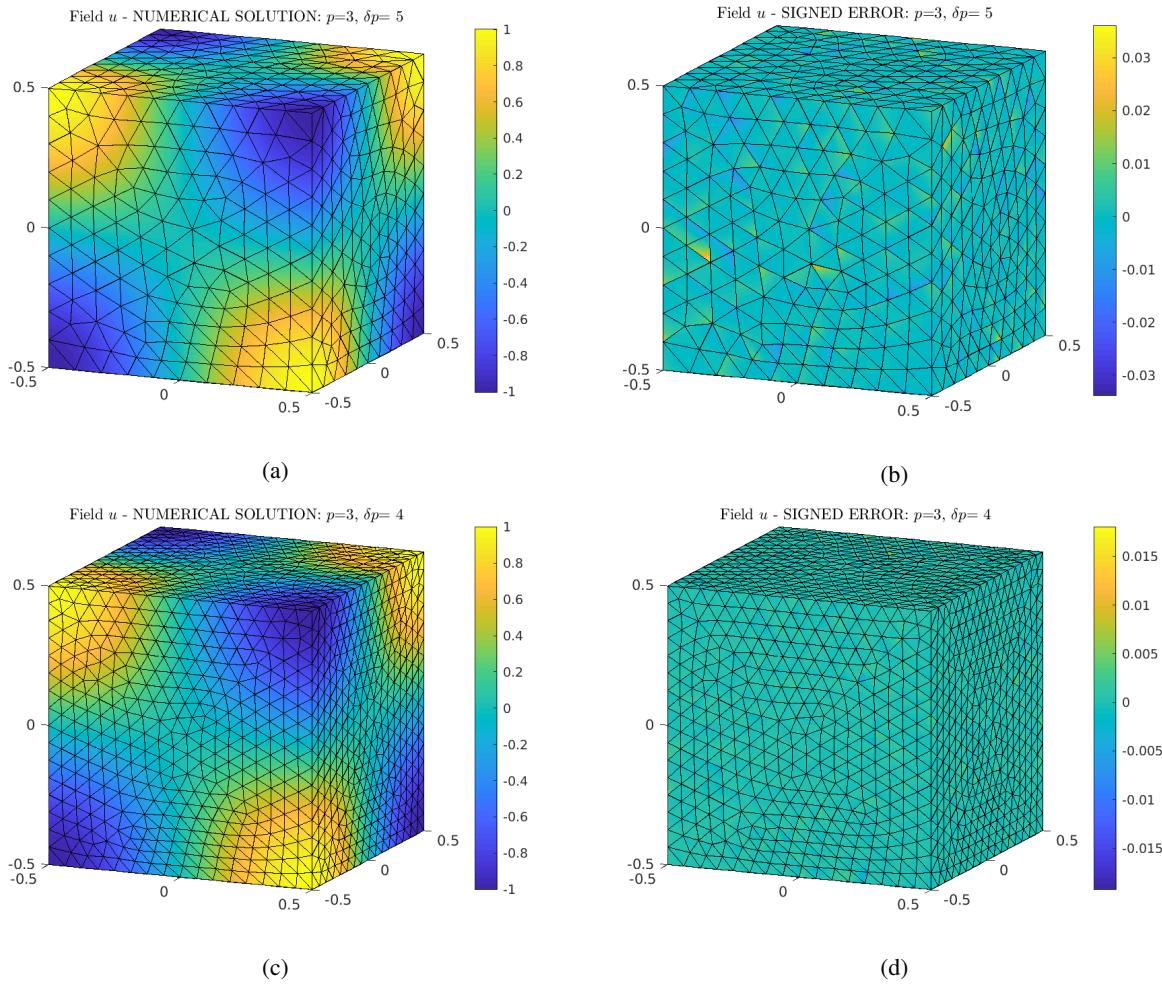


Figure 8.16: Sample plots of pointwise numerical solution (left) and signed error (right) for variable u_h in the agglomerated meshes of about 16 tetrahedra per element, with $p = 3$: (top) underlying mesh of 9462 tetrahedra with **discontinuous** discrete trace \hat{u}_h ; (bottom) underlying mesh of 27066 tetrahedra with **continuous** discrete trace \hat{u}_h .

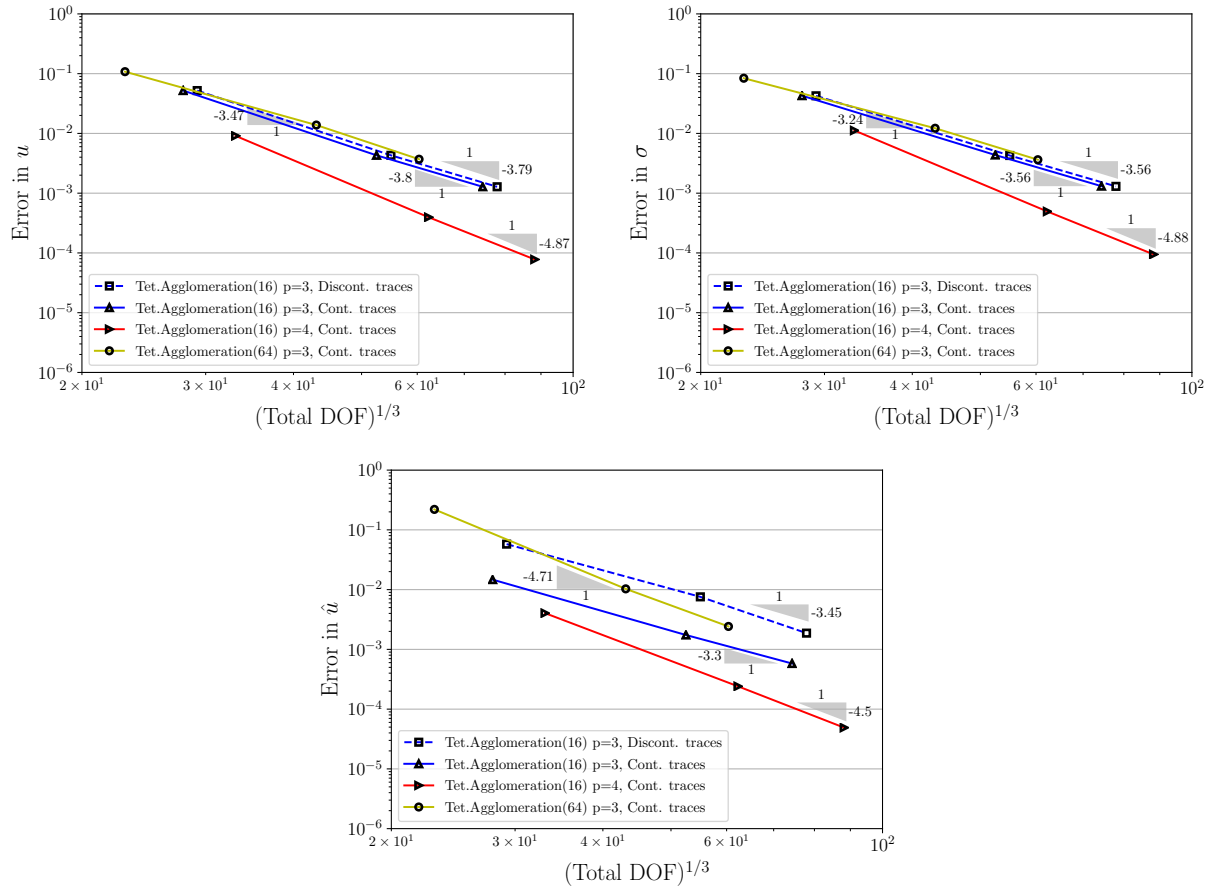


Figure 8.17: Error convergence in variables $(u_h, \sigma_h, \hat{u}_h)$ for the agglomerated mesh family utilizing p -enrichment, considering both discontinuous ($\delta p = 5$) and continuous ($\delta p = 4$) discretization of \hat{u} and $p = 3, 4$.

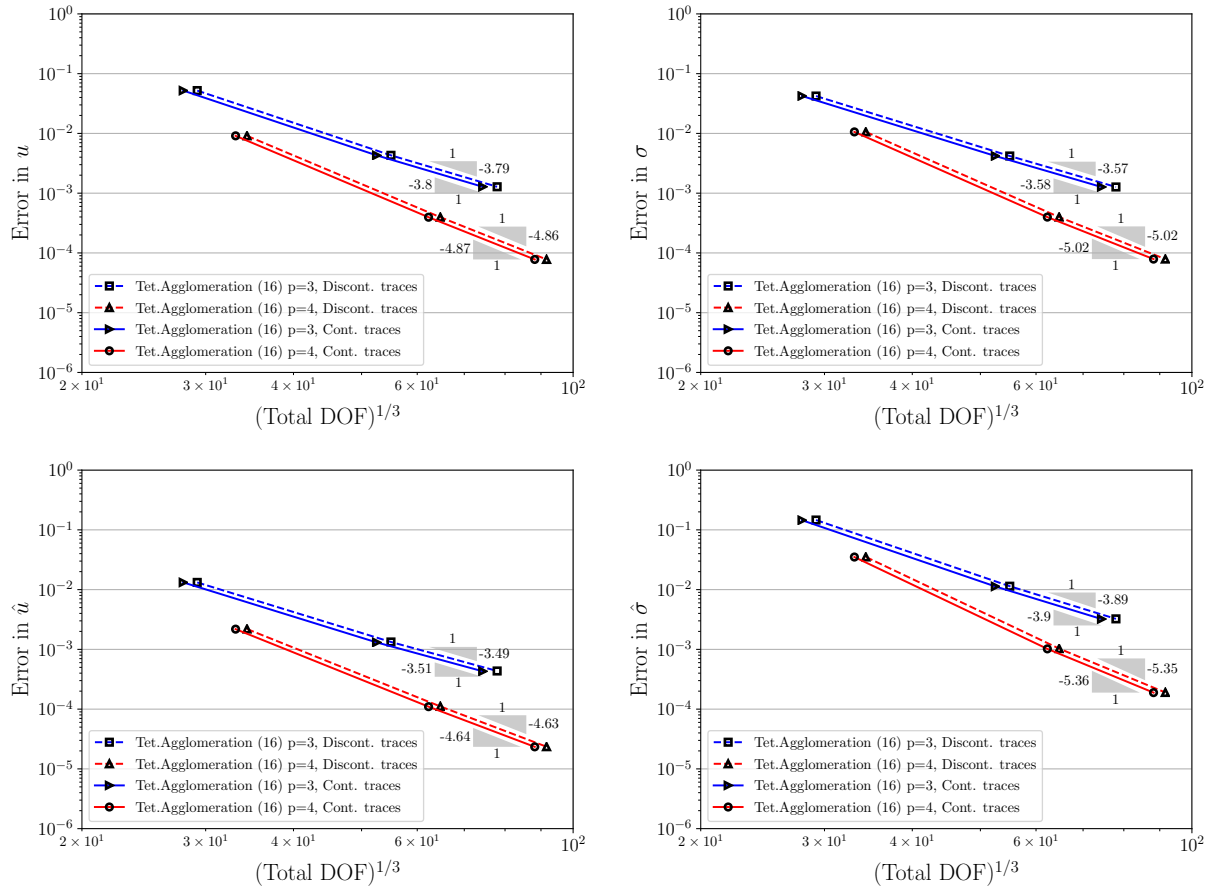


Figure 8.18: Error convergence in all variables for agglomerated meshes with 16 tetrahedra per element, for $p = 3, 4$ and hp -enrichment. Both discontinuous and continuous discretization of \hat{u} are considered.

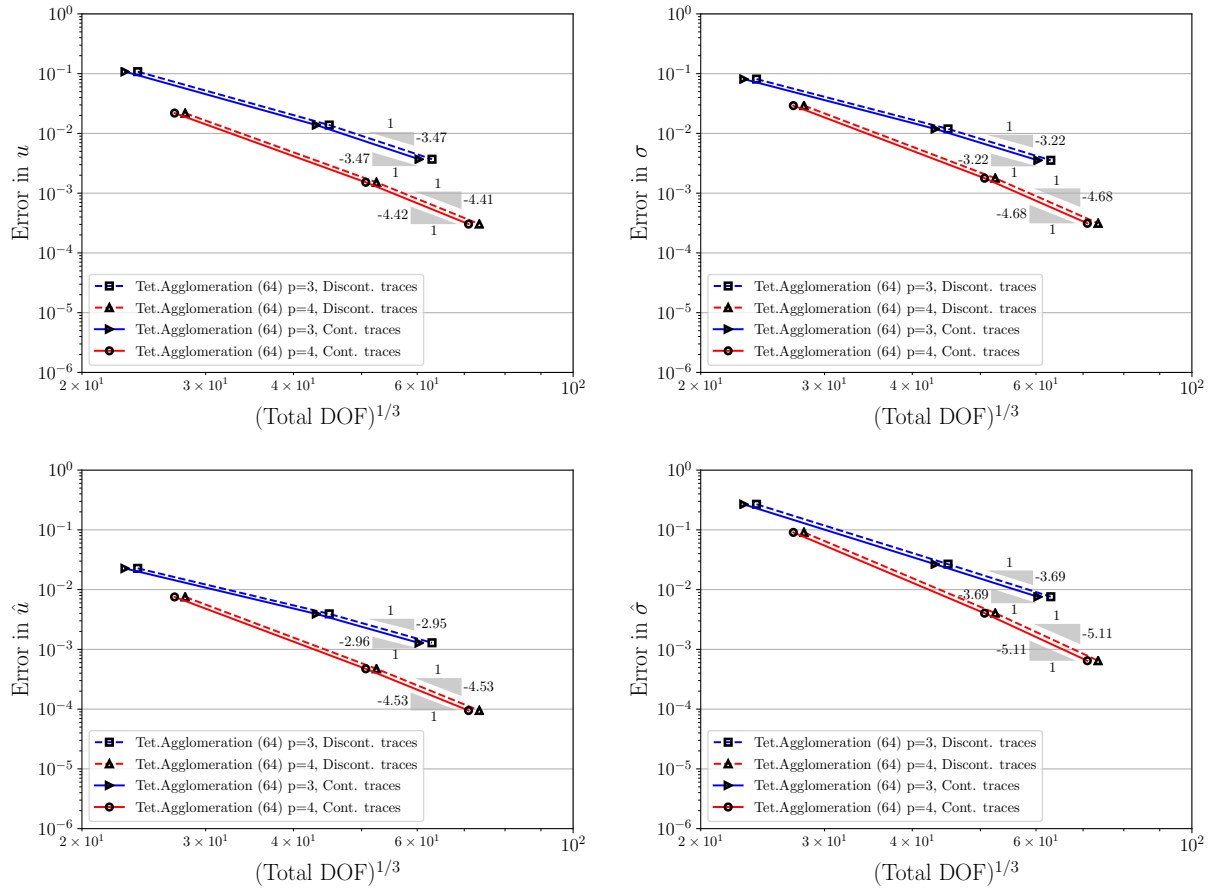


Figure 8.19: Error convergence in all variables for agglomerated meshes with 64 tetrahedra per element, for $p = 3, 4$ and hp -enrichment. Both discontinuous and continuous discretization of \hat{u} are considered.

traces get well approximated in some examples but fail to converge in several scenarios.

Regarding the test enrichment procedure, we have tried two options. Firstly, because of the homogeneous numerical integration, the p -enrichment proves to be an accurate and efficient choice when p is high and the number of faces is not very large. Moreover, if we are only interested in the field variables, this option may be appropriate even for a mesh of elements with many faces. The second option, hp -enrichment, involves a more complex implementation but it appears to be a better alternative whenever we are interested in a good approximation of the traces in meshes of more general element shapes (e.g., the agglomeration-based elements). The current limitation of this method is the cost of integration and the local computations, then it is practical only for a low or moderate order of approximation.

Finally, it has been important to include cases where the all the faces in the mesh have a standard shape (i.e., triangles) because we can compare the outcome of both the conforming and the non-conforming DPG methods. Notice that when the enrichment is sufficient, the quality of the numerical solutions of the continuous \hat{u}_h (conforming DPG) and discontinuous \hat{u}_h (non-conforming case) is almost identical, whether the elements are only tetrahedra (Figure 8.14) or agglomerated polyhedra (Figures 8.18 and 8.19).

Acknowledgments. L. Demkowicz and J. Mora-Paz were partially supported with NSF grant No. 1819101 and the Sandia exploratory LDRD project No. 19-1038, whose PI was Dr. Mohamed Ebeida, to whom we are deeply thankful. The first and last authors are grateful for an Oden Institute fellowship which allowed them to visit UT Austin in the Fall of 2019.

References

- [1] A. Abdelkader, C. L. Bajaj, M. S. Ebeida, A. H. Mahmoud, S. A. Mitchell, J. D. Owens, and A. A. Rushdi. Vorocrust: Voronoi meshing without clipping. *arXiv preprint arXiv:1902.08767*, 2019.
- [2] F. Bassi, L. Botti, A. Colombo, D. A. Di Pietro, and P. Tesini. On the flexibility of agglomeration based physical space discontinuous galerkin discretizations. *J. Comput. Phys.*, 231(1):45–65, 2012.
- [3] L. Beirão da Veiga, F. Brezzi, A. Cangiani, G. Manzini, LD Marini, and A. Russo. Basic principles of virtual element methods. *Math. Models Methods Appl. Sci.*, 23(01):199–214, 2013.
- [4] L. Beirão da Veiga, F. Brezzi, F. Dassi, LD Marini, and A. Russo. Virtual element approximation of 2d magnetostatic problems. *Comput. Methods Appl. Mech. Engrg.*, 327:173–195, 2017.
- [5] L. Beirão Da Veiga, F. Brezzi, L.D. Marini, and A. Russo. $H(\text{div})$ and $H(\text{curl})$ -conforming virtual element methods. *Numer. Math.*, 133(2):303–332, 2016.
- [6] L. Beirão da Veiga, F. Brezzi, L.D. Marini, and A. Russo. Virtual element method for general second-order elliptic problems on polygonal meshes. *Math. Models Methods Appl. Sci.*, 26(04):729–750, 2016.

- [7] Matias Fernando Benedetto, Stefano Berrone, Sandra Pieraccini, and Stefano Scialò. The virtual element method for discrete fracture network simulations. *Comput. Methods Appl. Mech. Engrg.*, 280:135–156, 2014.
- [8] J. E. Bishop. A displacement-based finite element formulation for general polyhedra using harmonic shape functions. *Int. J. Num. Meth. in Eng.*, 97(1):1–31, 2014.
- [9] J. E. Bishop. Applications of Polyhedral Finite Elements in Solid Mechanics. In *Generalized Barycentric Coordinates in Computer Graphics and Computational Mechanics*, pages 179–196. CRC Press, 2017.
- [10] F. Brezzi, K. Lipnikov, and V. Simoncini. A family of mimetic finite difference methods on polygonal and polyhedral meshes. *Math. Models Methods Appl. Sci.*, 15(10):1533–1551, 2005.
- [11] F. Brezzi and L. D. Marini. Virtual element methods for plate bending problems. *Comput. Methods Appl. Mech. Engrg.*, 253:455–462, 2013.
- [12] A. Cangiani, E. H. Georgoulis, and P. Houston. *hp*-Version discontinuous Galerkin methods on polygonal and polyhedral meshes. *Math. Models Methods Appl. Sci.*, 24(10):2009–2041, 2014.
- [13] C. Carstensen, L. Demkowicz, and J. Gopalakrishnan. Breaking spaces and forms for the DPG method and applications including Maxwell equations. *Comput. Math. Appl.*, 72(3):494–522, 2016.
- [14] S. N. Chandler-Wilde, D. P. Hewett, and A. Moiola. Interpolation of Hilbert and Sobolev spaces: Quantitative estimates and counterexamples. *Mathematika*, 61:414–443, 2014.
- [15] L. Chen, H. Wei, and M. Wen. An interface-fitted mesh generator and virtual element methods for elliptic interface problems. *J. Comput. Phys.*, 334(1):327–348, 2017.
- [16] H. Chi, L. Beirão da Veiga, and G. H. Paulino. Some basic formulations of the virtual element method (VEM) for finite deformations. *Comput. Methods Appl. Mech. Engrg.*, 318:148–192, 2017.
- [17] H. Chi, C. Talischi, O. Lopez-Pamies, and G. H. Paulino. Polygonal finite elements for finite elasticity. *Int. J. Num. Meth. in Eng.*, 101(4):305–328, 2015.
- [18] E. B. Chin, J. B. Lasserre, and N. Sukumar. Numerical integration of homogeneous functions on convex and nonconvex polygons and polyhedra. *Comput. Mech.*, 56(6):967–981, 2015.
- [19] B. Cockburn. Static condensation, hybridization, and the devising of the HDG methods. In G. R. Barrenechea, F. Brezzi, A. Cangiani, and E. H. Georgoulis, editors, *Building Bridges: Connections and Challenges in Modern Approaches to Numerical Partial Differential Equations*, volume 114 of *Lecture Notes in Computational Science and Engineering*, pages 129–177. Springer, Cham, 2016.
- [20] J. Collis and P. Houston. Adaptive discontinuous Galerkin methods on polytopic meshes. In *Advances in Discretization Methods*, pages 187–206. Springer, 2016.

- [21] L. Da Veiga Beirão, F. Brezzi, and L. D. Marini. Virtual elements for linear elasticity problems. *SIAM J. Numer. Anal.*, 51(2):794–812, 2013.
- [22] L. Demkowicz. Various variational formulations and Closed Range Theorem. Technical report, ICES, January 15–03.
- [23] L. Demkowicz. Lecture notes on Energy Spaces. Technical Report 13, ICES, 2018.
- [24] L. Demkowicz. Construction of DPG Fortin operators revisited. Technical Report 14, Oden Institute, August 2019.
- [25] L. Demkowicz and A. Buffa. H^1 , $H(\text{curl})$ and $H(\text{div})$ -conforming Projection-Based Interpolation in three dimensions. Quasi-optimal p -interpolation estimates. *Comput. Methods Appl. Mech. Engrg.*, 194:267–296, 2005.
- [26] L. Demkowicz and J. Gopalakrishnan. Analysis of the DPG method for the Poisson problem. *SIAM J. Num. Anal.*, 49(5):1788–1809, 2011. see also ICES Report 2010/37.
- [27] L. Demkowicz and J. Gopalakrishnan. *Recent Developments in Discontinuous Galerkin Finite Element Methods for Partial Differential Equations* (eds. X. Feng, O. Karakashian, Y. Xing), volume 157, chapter An Overview of the DPG Method, pages 149–180. IMA Volumes in Mathematics and its Applications, 2014.
- [28] L. Demkowicz, J. Kurtz, D. Pardo, M. Paszyński, W. Rachowicz, and A. Zdunek. *Computing with hp Finite Elements. II. Frontiers: Three-Dimensional Elliptic and Maxwell Problems with Applications*. Chapman & Hall/CRC, October 2007.
- [29] L. Demkowicz, P. Monk, L. Vardapetyan, and W. Rachowicz. De Rham diagram for hp finite element spaces. *Comput. Math. Appl.*, 39(7-8):29–38, 2000.
- [30] J. Droniou, R. Eymard, T. Gallouët, and R. Herbin. A unified approach to mimetic finite difference, hybrid finite volume and mixed finite volume methods. *Math. Models Methods Appl. Sci.*, 20(2):265–295, 2010.
- [31] J. Ernesti and C. Wieners. A space-time discontinuous Petrov-Galerkin method for acoustic waves. *Space-Time Methods. Applications to Partial Differential Equations*, pages 99–127, 2019.
- [32] F. Fuentes, B. Keith, L. Demkowicz, and S. Nagaraj. Orientation embedded high order shape functions for the exact sequence elements of all shapes. *Comput. Math. Appl.*, 70:353–458, 2015.
- [33] A. L. Gain, G. H. Paulino, L. S. Duarte, and I. Menezes. Topology optimization using polytopes. *Comput. Methods Appl. Mech. Engrg.*, 293:411–430, 2015.
- [34] A. Gillette, A. Rand, and C. Bajaj. Construction of scalar and vector finite element families on polygonal and polyhedral meshes. *Comput. Methods Appl. Math.*, 16(4):667–683, 2016.

- [35] J. Gopalakrishnan and W. Qiu. An analysis of the practical DPG method. *Math. Comp.*, 83(286):537–552, 2014.
- [36] N. Heuer, M. Karkulik, and F.-J. Sayas. Note on discontinuous trace approximation in the practical DPG method. *Comp. Math. Appl.*, 68:1562–1568, 2014.
- [37] G. Karypis and V. Kumar. A fast and high quality multilevel scheme for partitioning irregular graphs. *SIAM Journal on scientific Computing*, 20(1):359–392, 1998.
- [38] Y. Kuznetsov, K. Lipnikov, and M. Shashkov. The mimetic finite difference method on polygonal meshes for diffusion-type problems. *Comput. Geosci.*, 8(4):301–324, 2004.
- [39] J. Lasserre. Integration on a convex polytope. *Proceedings of the American Mathematical Society*, 126(8):2433–2441, 1998.
- [40] G. Manzini, A. Russo, and N. Sukumar. New perspectives on polygonal and polyhedral finite element methods. *Math. Models Methods Appl. Sci.*, 24(08):1665–1699, 2014.
- [41] W. McLean. *Strongly Elliptic Systems and Boundary Integral Equations*. Cambridge University Press, 2000.
- [42] S.E. Mousavi and N. Sukumar. Numerical integration of polynomials and discontinuous functions on irregular convex polygons and polyhedrons. *Comput. Mech.*, 47(5):535–554, 2011.
- [43] L. Mu, J. Wang, and X. Ye. Weak galerkin finite element methods on polytopal meshes. *arXiv preprint arXiv:1204.3655*, 2012.
- [44] S. Nagaraj, S. Petrides, and L. Demkowicz. Construction of DPG Fortin operators for second order problems. *Comput. Math. Appl.*, 74(8):1964–1980, 2017.
- [45] M. Peric and S. Ferguson. The advantage of polyhedral meshes. *Dynamics*, 24:45, 2005.
- [46] A. Rand, A. Gillette, and C. Bajaj. Quadratic serendipity finite elements on polygons using generalized barycentric coordinates. *Math. Comput.*, 83(290):2691–2716, 2014.
- [47] D. W. Spring, S. E. Leon, and G. H. Paulino. Unstructured polygonal meshes with adaptive refinement for the numerical simulation of dynamic cohesive fracture. *Int. J. Fract.*, 189(1):33–57, 2014.
- [48] E.M. Stein. *Singular Integrals and Differentiability Properties of Functions*. Princeton University Press, 1970.
- [49] A. Tabarraei and N. Sukumar. Application of polygonal finite elements in linear elasticity. *Int. J. Comput. Methods*, 3(04):503–520, 2006.
- [50] A. Tabarraei and N. Sukumar. Adaptive computations using material forces and residual-based error estimators on quadtree meshes. *Comput. Methods Appl. Mech. Engrg.*, 196(25):2657–2680, 2007.

- [51] C. Talischi, G. H. Paulino, A. Pereira, and I. Menezes. Polygonal finite elements for topology optimization: a unifying paradigm. *Int. J. Num. Meth. in Eng.*, 82(6):671–698, 2010.
- [52] A. Vaziri Astaneh, J. Mora Paz, F. Fuentes, and L. Demkowicz. High-order polygonal discontinuous Petrov-Galerkin (PolyDPG) using ultraweak formulations. *Comput. Methods Appl. Mech. Engrg.*, 332:686–711, 2018.
- [53] E. Wachspress. *A Rational Finite Element Basis*. Mathematics in Science and Engineering. Elsevier Science, 1975.

A Construction of Fortin Operators

Construction of $H(\text{div})$ interpolation operator on master tetrahedron \check{T} . Let $\mathcal{RT}^{p+1}(\check{T})$ denote the Raviart-Thomas space of polynomials of order $p+1$ defined on master tetrahedron \check{T} . We begin by recalling the construction of the Raviart-Thomas $H(\text{div})$ interpolation operator.

$$\begin{aligned} \check{\Pi}^{\text{div}} : H^\epsilon(\text{div}, \check{T}) &\rightarrow \mathcal{RT}^{p+1}(\check{T}), \quad \tau \rightarrow \tau_p \\ \left\{ \begin{array}{ll} \langle (\tau_p - \tau) \cdot n, \phi \rangle = 0 & \forall \phi \in \mathcal{P}^p(F) \quad \text{for each face } F \text{ of } \check{T} \\ (\tau_p - \tau, \psi) = 0 & \forall \psi \in \mathcal{P}^{p-1}(\check{T}) \end{array} \right. \end{aligned} \quad (\text{A.39})$$

The operator commutes with the L^2 -projection onto $\mathcal{P}^p(\check{T})$,

$$\begin{array}{ccc} H^\epsilon(\text{div}, \check{T}) & \xrightarrow{\text{div}} & H^\epsilon(\check{T}) \\ \downarrow \check{\Pi}^{\text{div}} & & \downarrow \check{P} \\ \mathcal{RT}^{p+1}(\check{T}) & \xrightarrow{\text{div}} & \mathcal{P}^p(\check{T}). \end{array}$$

The finite-dimensionality argument implies that operator $\check{\Pi}^{\text{div}}$ is continuous on the space $H^\epsilon(\text{div}, \check{T})$.

Construction of $H(\text{div})$ interpolation operator on an arbitrary tetrahedron. Let T be now an affine map from master tetrahedron \check{T} onto an arbitrary tetrahedron T , $x = T\xi = A\xi + b$, $j = \det A$. We employ the standard Piola transforms for integer norms,

$$\begin{aligned} \Phi_{\text{div}} : H(\text{div}, \check{K}) &\rightarrow H(\text{div}, K), & \check{\tau} &\rightarrow \tau, & \tau(x) &= A\check{\tau}(\xi)/j \\ \Phi_{L^2} : L^2(\check{K}) &\rightarrow L^2(K), & \check{f} &\rightarrow f & f(x) &= \check{f}(\xi)/j \end{aligned}$$

The Raviart-Thomas interpolation operator defined on $H^\epsilon(\text{div}, K)$ is defined as follows,

$$P^{\text{div}} \tau := \Phi_{\text{div}} \check{P}^{\text{div}} \check{\tau} = \Phi_{\text{div}} \check{P}^{\text{div}} \Phi_{\text{div}}^{-1} \tau. \quad (\text{A.40})$$

Let $P : L^2(T) \rightarrow \mathcal{P}^p(T)$ be the orthogonal projection. The use of the Piola transforms implies that

$$\text{div} P^{\text{div}} \tau = P \text{div} \tau = \Phi_{L^2} \widetilde{\text{div}} \check{\tau}.$$

Construction of $H(\text{div})$ Fortin operator for an arbitrary tetrahedron. We start by studying the scaling properties of the broken fractional norm for general elements:

$$\|\tau\|_{H^\epsilon(\mathcal{T}_h)}^2 := \sum_{K \in \mathcal{T}_h} \left(\|\tau\|^2 + |\tau|_{H^\epsilon(K)}^2 + \|\text{div}\tau\|^2 + |\text{div}\tau|_{H^\epsilon(K)}^2 \right).$$

For a simple scaling, $x = h\xi + x_0$, using the Piola transform for L^2 -functions, we have,

$$\begin{aligned} \|f\|_{H^\epsilon(K)}^2 &= \int_K |f(x)|^2 dx + \int_K \int_K \frac{|f(x) - f(y)|^2}{|x - y|^{3+2\epsilon}} dx dy \\ &= h^{-3} \int_{\tilde{K}} |\check{f}(\xi)|^2 d\xi + h^{-3-2\epsilon} \int_{\tilde{K}} \int_{\tilde{K}} \frac{|\check{f}(\xi) - \check{f}(\eta)|^2}{|\xi - \eta|^{3+2\epsilon}} d\xi d\eta \\ &\leq h^{-3-2\epsilon} \|\check{f}\|_{H^\epsilon(\tilde{K})}^2. \end{aligned}$$

The result extends to general affine elements under standard shape regularity assumptions. Similarly, using the Piola transform for $H(\text{div})$ -space, we obtain

$$\|\tau\|_{H^\epsilon(K)}^2 \lesssim h^{-1-2\epsilon} \|\check{\tau}\|_{H^\epsilon(\tilde{K})}^2.$$

Now, assuming every element K corresponds to some tetrahedron T , the scaling properties imply the continuity of the Raviart-Thomas-Fortin operator:

$$\begin{aligned} \|\Pi^{\text{div}}\tau\|_{H^\epsilon(T)}^2 &= \|\Phi_{\text{div}}\check{P}^{\text{div}}\check{\tau}\|_{H^\epsilon(T)}^2 \lesssim h^{-1-2\epsilon} \|\check{P}^{\text{div}}\check{\tau}\|_{H^\epsilon(\tilde{T})}^2 \\ &\lesssim h^{-1-2\epsilon} \|\check{P}^{\text{div}}\| \|\check{\tau}\|_{H^\epsilon(\tilde{T})}^2 \lesssim h^{-2\epsilon} \|\check{P}^{\text{div}}\| \|\tau\|_{H^\epsilon(T)}^2 \\ \|\text{div}\Pi^{\text{div}}\tau\|_{H^\epsilon(T)}^2 &= \|P^{\text{div}}\tau\|_{H^\epsilon(T)}^2 \lesssim h^{-3-2\epsilon} \|\check{P}^{\text{div}}\check{\tau}\|_{H^\epsilon(\tilde{T})}^2 \\ &\lesssim h^{-3-2\epsilon} \|\check{P}\| \|\check{\text{div}}\check{\tau}\|_{H^\epsilon(\tilde{T})}^2 \lesssim h^{-2\epsilon} \|\check{P}\| \|\text{div}\tau\|_{H^\epsilon(T)}^2. \end{aligned}$$

where $\|\check{P}^{\text{div}}\|, \|\check{P}\| = 1$ are the norms of the Raviart-Thomas interpolation operator and L^2 -projection on the master element. Note that constant $\|\check{P}^{\text{div}}\|$ blows up with $\epsilon \rightarrow 0$ as the definition of operator for $\epsilon = 0$ is illegal. Combining the estimates, we obtain,

$$\|\Pi^{\text{div}}\tau\|_{H^\epsilon(\text{div},T)} \lesssim h^{-\epsilon} \|\check{P}^{\text{div}}\| \|\tau\|_{H^\epsilon(\text{div},T)}. \quad (\text{A.41})$$

Construction of $H(\text{div})$ and H^1 Fortin operators for an arbitrary polyhedron covered with a shape regular subelement tetrahedral mesh. Generalization of the construction discussed above to an arbitrary polyhedron depends strongly upon the definition of the enriched space which in turns depends clearly upon the number of faces. The choice of an appropriate polynomial enriched space and the construction of the corresponding Fortin operator are certainly challenging tasks.

We can collect though a ‘‘low hanging fruit’’. If the polyhedron can be covered with a shape-regular subelement tetrahedral mesh, we can employ the piecewise-polynomial $H(\text{div})$ -conforming space of order $p + 1$ defined on the tetrahedral submesh, and the corresponding discussed Raviart-Thomas interpolation

operator for the Fortin operator. Under the shape regularity for the submesh elements, the continuity properties remain intact. The operator satisfies the desired orthogonality properties for each subelement which implies that they are satisfied for the whole element as well.

The same idea applies to the H^1 Fortin operator. One can utilize any of the Fortin operators constructed in [35, 13, 44, 24] for the submesh elements.